Journal of Geophysical Research: Solid Earth

RESEARCH ARTICLE

Key Points:
- Two-dimensional planar isoviscous mixed heating scaling extended to 3-D spherical
- Internal temperatures and heat flow are well described
- Boundary layers, velocities, and temperature gradients diverge from theory

Correspondence to:
M. B. Weller,
mbweller@ig.utexas.edu

Scaling relationships and physics for mixed heating convection in planetary interiors: Isoviscous spherical shells

Matthew B. Weller[1,2,3], Adrian Lenardic[1], and William B. Moore[4,5]

[1]Department of Earth Science, Rice University, Houston, Texas, USA, [2]Lunar and Planetary Institute, Houston, Texas, USA, [3]Now at Institute for Geophysics, University of Texas at Austin, Austin, Texas, USA, [4]Department of Atmospheric and Planetary Sciences, Hampton University, Hampton, Virginia, USA, [5]National Institute of Aerospace, Hampton, Virginia, USA

Abstract We use a suite of 3-D numerical experiments to test and expand 2-D planar isoviscous scaling relationships of Moore (2008) for mixed heating convection in spherical geometry mantles over a range of Rayleigh numbers (*Ra*). The internal temperature scaling of Moore (2008), when modified to account for spherical geometry, matches our experimental results to a high degree of fit. The heat flux through the boundary layers scale as a linear combination of internal (*Q*) and basal heating, and the modified theory predictions match our experimental results. Our results indicate that boundary layer thickness and surface heat flux are not controlled by a local boundary layer stability condition (in agreement with the results of Moore (2008)) and are instead strongly influenced by boundary layer interactions. Subadiabatic mantle temperature gradients, in spherical 3-D, are well described by a vertical velocity scaling based on discrete drips as opposed to a scaling based on coherent sinking sheets, which was found to describe 2-D planar results. Root-mean-square (RMS) velocities are asymptotic for both low *Q* and high *Q*, with a region of rapid adjustment between asymptotes for moderate *Q*. RMS velocities are highest in the low *Q* asymptote and decrease as internal heating is applied. The scaling laws derived by Moore (2008), and extended here, are robust and highlight the importance of differing boundary layer processes acting over variable *Q* and moderate *Ra*.

1. Introduction

The Earth's mantle is heated by a combination of internal heating, from the decay of radioactive nuclei, and basal heating associated with core cooling. This is also the case for other terrestrial planets and moons in the solar system (for satellites such as Io, Europa, Enceladus, and perhaps the young Earth-Moon system, internal heating is linked principally to tidal effects as opposed to radiogenic heating). The surface and basal heat flux of a planet depends on the combination of these heating modes, and an understanding of planetary heat transfer properties, as a function of internal and basal heating levels, is critical to developing thermal history models for terrestrial planets.

While many studies have modeled the thermal evolution of planetary mantles, until relatively recently, the majority of attention has been focused on the end-member parameterization of internal or basal heating only [e.g., *Reese et al.*, 1999; *Hauck and Phillips*, 2002; *Reese et al.*, 2005]. Recently, there has been an increased interest in exploring mixed heating systems [*Sotin and Labrosse*, 1999; *Moore*, 2008; *Shahnas et al.*, 2008; *Choblet and Parmentier*, 2009; *Wolstencroft et al.*, 2009; *Deschamps et al.*, 2010; *O'Farrell and Lowman*, 2010; *Deschamps et al.*, 2012; *O'Farrell et al.*, 2013]. Several of the most recent studies have analyzed mixed heating convective systems using inversion techniques applied to the output from numerical convection experiments [e.g., *Deschamps et al.*, 2012; *O'Farrell et al.*, 2013]. The inversion techniques seek to uncover empirical scaling relationships between key model parameters. An alternative approach is to start with theoretically derived scaling relationships and use numerical experiments to test the validity and map the limits of the theoretical framework. That latter approach is the one we follow herein.

The goal of this study is to evaluate and expand the theoretical scaling relationships of *Moore* [2008]. The theory was developed for a 2-D planar system, which is designed to emulate physical tank experiments. We extend it to address a 3-D spherical shell system, designed to emulate planetary interiors. We then use a large suite of numerical experiments to test the theoretical scaling predictions. We focus on isoviscous systems in order to test the scaling theory as straight forwardly, and comparably, as possible. We will extend the theory to include temperature- and depth-dependent viscosities, as well as surface yielding in future work.

2. Models and Methods

The governing equations of mass, momentum, and energy conservation, assuming infinite Prandtl number and Boussinesq fluid approximation, are given in nondimensional form by

$$u_{i,i} = 0 \tag{1}$$

$$-P_{,i} + \left(\eta\left(u_{i,j} + u_{j,i}\right)\right)_{,j} + RaT\delta_{ir} = 0 \tag{2}$$

$$T_{,t} + u_i T_{,i} = T_{,ii} + Q, \tag{3}$$

where u is the velocity, P is the dynamic pressure, η is the viscosity, Ra is the Rayleigh number, T is temperature, δ_{ij} is the Kroneker delta tensor, Q is the heat production rate, i and j represent spatial indices, r is a unit vector in the radial direction, t is time, and the form $X_{,y}$ represents the derivative of X with respect to y. Repeated indices imply summation. Equations (1)–(3) are solved using the community benchmark code CitcomS (version 3.2) [e.g., *Zhong et al.*, 2000; *Tan et al.*, 2006].

The vigor of convection is described by the Ra:

$$Ra = g\rho\alpha\Delta T d^3/(\kappa\eta), \tag{4}$$

where α is the thermal expansivity, ρ is density, g is gravity, κ is the thermal diffusivity, d is layer depth, and η is the viscosity. ΔT is the reference temperature drop across the system, given as follows: the temperature contrast from the base of the convecting layer to the surface (T_s–T_b). CitcomS uses a Ra based on full shell convection (d = planetary radius R_0), thereby requiring a modification of the full radius Ra (Ra_{R_0}) to an effective Ra (Ra_{eff}) to account for convection in the thinner layer: $Ra_{eff} = (R_0 - f)^{-3}Ra_{R_0}$, where $f = R_c/R_0$ and R_c is the core radius. R_c and R_0 are taken as nondimensional (see CitcomS user manual; https://geodynamics.org/cig/software/github/citcoms/v3.2.0/citcoms-3.2.0-manual.pdf). For the remainder of this paper, Ra_{eff} will be shortened to Ra unless otherwise noted. Additional critical nondimensional quantities are the internal heat generation rate Q:

$$Q = Hd^2/(\kappa\Delta T), \tag{5}$$

where H is the volumetric heating rate.

We run suites of numerical experiments with Q varying between [0 – 200] and Ra varying between 2 orders of magnitude [1e5–1e7], with higher values of Q associated with higher values of Ra. Similar Q values were selected as comparison points between differing Ra values. Each simulation was run to a time that allows for a statistically steady state and then allowed to run twice that length where computationally favorable (e.g., lower Ra simulations). Where computationally prohibitive (e.g., high Ra systems), simulations were run to a time that allows for a statistically steady state then run ~15–30% longer. Model resolution was not assumed a priori; as a result, varying model resolutions were tested with system tie points at specific Q and Ra values. Model domains consist of 32, 65, 81, or 128 grid cell elements in the three primary directions for each of the 12 spherical caps. Boundary conditions are free slip; basal and surface temperatures are fixed (T_b = 1; T_s = 0) and f = 0.55.

3. Geometric Factors

For use with thermal history calculations, the boundary heat flow needs to be expressed as a function of the convective parameters Ra and Q. At statistically steady state, convective systems must balance heat input and output. The Nusselt number (Nu) is a useful nondimensional representation of heat flow. In the planar case, the balance between basal and surface Nu and internal heating rate is given by

$$Nu_{surf} = Nu_{bot} + Q \tag{6}$$

It has been long known that correction factors accounting for different geometries, areas, and volumes in spherical domains should be implemented in order to scale between experiments and/or theory in planar versus spherical systems [e.g., *Shahnas et al.*, 2008; *O'Farrell and Lowman*, 2010; *Deschamps et al.*, 2010; *Choblet*, 2012; *Deschamps et al.*, 2012; *O'Farrell et al.*, 2013].

The manner in which CitcomS nondimensionalizes model equations will lead to a specific form of a geometric correction. We follow the approach of the codes principal author [*Zhong et al.*, 2008; S. Zhong,

personal communication, 2015], which starts by solving the steady state heat equation in spherical geometry for a shell. This leads to a modified form of equation (6):

$$q'_{surf} \frac{(1-f)}{f} = q'_{bot}(1-f)f + \frac{(1-f^3)}{3}\frac{(1-f)}{f}Q,$$ (7)

where $Nu_{surf} = (1-f)f^{-1}q'_{surf}$ and $Nu_{bot} = (1-f)fq'_{bot}$ and assuming $\Delta T = 1$. Q and the product of the term adjacent to Q can be thought of as giving an effective Q (Q_{eff}):

$$Q_{eff} = \frac{(1-f^3)}{3}\frac{(1-f)}{f}Q$$ (8)

An inspection of equation (7) suggests that the top and bottom boundary heat fluxes as well as Q should be scaled together. It is useful to consider end-members. At $f = 1$, equation (7) predicts all quantities to be 0. At $f = 0$, equation (7) breaks down. The implication of $f = 1$ is a sphere whose inner boundary is equal to its outer boundary. To put it another way, there is no convecting layer, only the basal boundary. Consequently, the prediction of equation (7) is one of returning a shell heat flow of 0. For $f = 0$, the opposite condition occurs, there is no bottom boundary, only the convecting layer. As a result the assumption of both a finite f and $\Delta T = 1$ that were used in the derivation of the scaling form of equation (7) are invalid. For all f between the conceptual end-members of zero and one, energy is conserved, which is the principal requirement of a geometric correction [e.g., *Deschamps et al.*, 2010, 2012].

We present our results as parameterizations of heat flow and temperature structure within a spherical shell for a range of mixed, basal, and internal heating conditions for isoviscous convection. The results of 98 three-dimensional numerical experiments are summarized in Table 1. Data analyses in the following sections are limited to cases where the maximum misfits in the energy balance fall below 2.84% (where misfits are reported as percent differences). The remainder of the discussion will report Q in terms of CitcomS input parameters. The reader is referred back to Table 1 to reference Q to Q_{eff}. The temperature and root-mean-square (RMS) velocity structure within the shell are computed from both horizontal and time averages of the internal temperature and velocity fields ($<>$ denotes time averages). The temperature domain is radially divided into the average temperature of the upper mantle $<T_{um}>$ and lower mantle $<T_i>$. $<T_{um}>$ is taken from $R = 0.95$ to $R = 0.85$, and $<T_i>$ is taken from $R = 0.85$ to $R = 0.55$, where $R = 0.55$ is the base of the system, giving a mantle depth of 0.45. The value of $<T_i>$ is consistent with the definition used in *Moore* [2008].

4. Internal Temperatures

The inclusion of heat production within the mantle requires more heat to be transported through the upper boundary layer [e.g., *Sotin and Labrosse*, 1999; *Moore*, 2008; *Deschamps et al.*, 2010]. This is accommodated by an increase in the internal temperature, which leads to an increase in the temperature drop across the upper thermal boundary layer (approximated by T_{um}). However, for large internal heating rates (resulting in large internal temperatures), this excess heat may not only be transported through the upper boundary layer but also through the lower boundary layer. The effects of internal heat production on internal temperatures are additive to the basally heated reference case. Therefore, both T_{um} and T_i (time average notation dropped for simplicity) should both follow the form of $T = T_{bh} + cQ^{3/4}Ra^{-1/4}$, where T_{bh} is the reference basal heating temperature and c is a constant. This form follows

$$T_i = 0.228 + 1.184Q^{3/4}Ra^{-1/4}$$ (9a)

as shown in Figure 1. Equation (9a), with an $R^2 = 0.996$ is nearly identical to the results of *Moore* [2008], given as $T_i = 0.49 + 1.24Q^{3/4}Ra^{-1/4}$, where the variation in c (~4.5%) and T_{bh} (~47%) reflect the effects of 3-D spherical geometries. Further, the upper mantle temperature scales as

$$T_{um} = 0.223 + 1.335Q^{3/4}Ra^{-1/4}$$ (9b)

agreeing with the $\Delta T_{top} = 0.50 + 1.355Q^{3/4}Ra^{-1/4}$ of *Moore* [2008], with an $R^2 = 0.998$ (using an identical Ra range). The average variance in predicted to actual T_i is ~ 0.72% and T_{um} is ~0.69%. The difference in the base offset temperatures (~0.5 for planar and ~0.2 for spherical) is well known and expected given the change in domain geometry [e.g., *Schubert et al.*, 2001]. Consequently, these values are nearly indistinguishable from the results of *Sotin and Labrosse* [1999].

Table 1. Convection Results

Ra_{R0}	Ra_{eff}	Resolution	Q_{R0}	Q_{eff}	T_{um}	T_i	$T_{um} - T_i$	RMS Velocity	q_{surf}	q_{bot}	Nu_{surf}	Nu_{bot}	Misfit (%)
1.10e+06	1.00e+05	33 × 33 × 33	0	0.000	0.240	0.205	0.035	373.960	8.376	27.773	6.853	6.874	−0.351
1.10e+06	1.00e+05	33 × 33 × 33	10	2.274	0.351	0.330	0.020	380.440	11.019	27.084	9.016	6.703	0.490
1.10e+06	1.00e+05	65 × 65 × 65	10	2.274	0.348	0.328	0.020	379.370	11.217	27.787	9.178	6.877	0.330
1.10e+06	1.00e+05	33 × 33 × 33	30	6.821	0.521	0.515	0.006	329.320	15.944	24.651	13.045	6.101	1.029
1.10e+06	1.00e+05	65 × 65 × 65	30	6.821	0.510	0.503	0.007	330.720	16.004	25.264	13.094	6.253	0.171
1.10e+06	1.00e+05	33 × 33 × 33	50	11.368	0.694	0.668	0.026	268.680	20.055	19.533	16.409	4.834	1.352
1.10e+06	1.00e+05	33 × 33 × 33	60	13.641	0.768	0.730	0.038	251.260	22.060	16.988	18.049	4.205	1.200
1.10e+06	1.00e+05	33 × 33 × 33	80	18.188	0.899	0.840	0.059	235.150	26.233	12.473	21.463	3.087	0.922
1.10e+06	1.00e+05	33 × 33 × 33	100	22.735	1.013	0.933	0.080	226.890	30.576	8.554	25.017	2.117	0.688
1.10e+06	1.00e+05	33 × 33 × 33	120	27.282	1.123	1.024	0.099	225.060	35.062	5.088	28.687	1.259	0.527
1.10e+06	1.00e+05	33 × 33 × 33	140	31.829	1.230	1.111	0.118	222.970	39.617	1.836	32.414	0.454	0.416
3.29e+06	3.00e+05	33 × 33 × 33	0	0.000	0.255	0.229	0.025	719.370	11.956	39.535	9.782	9.785	−0.028
3.29e+06	3.00e+05	33 × 33 × 33	4	0.909	0.273	0.262	0.012	711.890	13.389	40.295	10.955	9.973	0.731
3.29e+06	3.00e+05	33 × 33 × 33	10	2.274	0.306	0.303	0.003	698.560	14.790	40.148	12.101	9.937	−0.979
3.29e+06	3.00e+05	65 × 65 × 65	10	2.274	0.307	0.302	0.004	685.590	15.291	41.192	12.511	10.195	0.370
3.29e+06	3.00e+05	33 × 33 × 33	12	2.728	0.325	0.324	0.001	675.230	14.997	38.644	12.270	9.564	−0.201
3.29e+06	3.00e+05	33 × 33 × 33	20	4.547	0.386	0.386	0.001	617.380	17.470	38.898	14.294	9.627	0.905
3.29e+06	3.00e+05	33 × 33 × 33	30	6.821	0.457	0.450	0.007	546.980	19.696	36.310	16.115	8.987	2.057
3.29e+06	3.00e+05	65 × 65 × 65	30	6.821	0.446	0.438	0.008	539.750	20.191	38.741	16.520	9.588	0.719
3.29e+06	3.00e+05	33 × 33 × 33	50	11.368	0.585	0.559	0.026	462.400	23.486	30.227	19.216	7.481	2.036
3.29e+06	3.00e+05	65 × 65 × 65	50	11.368	0.567	0.543	0.025	459.000	23.915	32.659	19.567	8.083	0.629
3.29e+06	3.00e+05	33 × 33 × 33	60	13.641	0.642	0.607	0.035	437.050	25.416	27.443	20.795	6.792	1.844
3.29e+06	3.00e+05	65 × 65 × 65	60	13.641	0.624	0.591	0.033	435.990	25.782	29.693	21.094	7.349	0.518
3.29e+06	3.00e+05	33 × 33 × 33	61	13.868	0.649	0.613	0.035	430.860	25.541	27.056	20.897	6.696	1.684
3.29e+06	3.00e+05	33 × 33 × 33	80	18.188	0.742	0.693	0.049	413.180	29.408	22.636	24.061	5.602	1.180
3.29e+06	3.00e+05	33 × 33 × 33	99	22.508	0.827	0.765	0.062	399.500	33.275	18.680	27.225	4.623	0.359
3.29e+06	3.00e+05	33 × 33 × 33	100	22.735	0.832	0.769	0.063	403.760	33.552	18.614	27.452	4.607	0.416
3.29e+06	3.00e+05	33 × 33 × 33	120	27.282	0.913	0.838	0.075	398.740	37.812	15.065	30.937	3.729	−0.246
3.29e+06	3.00e+05	65 × 65 × 65	120	27.282	0.901	0.824	0.077	379.300	38.562	16.823	31.551	4.164	0.345
3.29e+06	3.00e+05	65 × 65 × 65	120	27.282	0.901	0.825	0.076	381.730	38.598	16.920	31.580	4.188	0.360
3.29e+06	3.00e+05	33 × 33 × 33	148	33.648	1.019	0.927	0.093	391.440	43.747	10.312	35.793	2.552	−1.164
3.29e+06	3.00e+05	33 × 33 × 33	160	36.376	1.066	0.967	0.099	395.950	46.407	8.712	37.969	2.156	−1.513
3.29e+06	3.00e+05	65 × 65 × 65	180	40.923	1.126	1.013	0.113	372.640	52.282	6.897	42.776	1.707	0.349
6.58e+06	6.00e+05	33 × 33 × 33	0	0.000	0.247	0.237	0.009	1087.000	15.093	50.032	12.349	12.383	−0.299
6.58e+06	6.00e+05	65 × 65 × 65	0	0.000	0.206	0.197	0.009	1072.000	15.517	51.479	12.696	12.741	−0.384
6.58e+06	6.00e+05	33 × 33 × 33	10	2.274	0.306	0.305	0.001	1033.700	17.552	48.356	14.361	11.968	0.898
6.58e+06	6.00e+05	65 × 65 × 65	10	2.274	0.291	0.293	−0.002	1017.100	18.806	53.055	15.387	13.131	−0.122
6.58e+06	6.00e+05	33 × 33 × 33	30	6.821	0.427	0.418	0.009	762.230	22.139	43.871	18.114	10.858	2.577
6.58e+06	6.00e+05	65 × 65 × 65	30	6.821	0.417	0.410	0.007	758.440	23.465	49.572	19.199	12.269	0.603
6.58e+06	6.00e+05	33 × 33 × 33	50	11.368	0.528	0.504	0.024	658.800	25.758	37.809	21.075	9.358	1.757
6.58e+06	6.00e+05	33 × 33 × 33	60	13.641	0.574	0.544	0.030	631.270	27.619	35.122	22.597	8.693	1.226
6.58e+06	6.00e+05	33 × 33 × 33	80	18.188	0.657	0.615	0.042	596.250	31.427	30.369	25.713	7.516	0.034
6.58e+06	6.00e+05	33 × 33 × 33	100	22.735	0.732	0.680	0.052	582.370	35.359	26.386	28.930	6.531	−1.195
6.58e+06	6.00e+05	33 × 33 × 33	120	27.282	0.800	0.739	0.061	579.820	39.367	22.978	32.209	5.687	−2.407
6.58e+06	6.00e+05	65 × 65 × 65	120	27.282	0.800	0.738	0.061	545.330	41.542	26.248	33.989	6.496	0.640
6.58e+06	6.00e+05	33 × 33 × 33	140	31.829	0.864	0.794	0.070	579.320	43.364	19.844	35.480	4.911	−3.591
6.58e+06	6.00e+05	65 × 65 × 65	140	31.829	0.864	0.793	0.071	538.880	46.000	22.575	37.636	5.587	0.601
6.58e+06	6.00e+05	33 × 33 × 33	148	33.648	0.890	0.816	0.073	579.770	44.958	18.687	36.784	4.625	−4.077
6.58e+06	6.00e+05	65 × 65 × 65	148	33.648	0.889	0.815	0.074	539.220	47.824	21.213	39.129	5.250	0.607
6.58e+06	6.00e+05	33 × 33 × 33	160	36.376	0.925	0.847	0.078	580.860	47.331	16.905	38.725	4.184	−4.750
6.58e+06	6.00e+05	65 × 65 × 65	160	36.376	0.924	0.845	0.080	534.140	50.517	19.082	41.332	4.723	0.579
6.58e+06	6.00e+05	33 × 33 × 33	180	40.923	0.984	0.897	0.086	580.870	51.245	14.110	41.928	3.492	−5.899
6.58e+06	6.00e+05	65 × 65 × 65	180	40.923	0.985	0.896	0.089	531.560	55.059	15.686	45.048	3.882	0.552
6.58e+06	6.00e+05	65 × 65 × 65	200	45.470	1.044	0.946	0.098	527.860	59.647	12.555	48.802	3.107	0.470
1.10e+07	1.00e+06	33 × 33 × 33	0	0.000	0.231	0.221	0.010	1461.800	16.738	55.968	13.695	13.852	−1.229
1.10e+07	1.00e+06	65 × 65 × 65	0	0.000	0.219	0.209	0.010	1422.400	18.251	61.135	14.933	15.131	−1.411
1.10e+07	1.00e+06	81 × 81 × 81	0	0.000	0.200	0.196	0.004	1457.000	18.327	60.816	14.995	15.052	−0.406
1.10e+07	1.00e+06	65 × 65 × 65	10	2.274	0.290	0.292	−0.001	1370.600	21.852	63.038	17.879	15.602	0.021
1.10e+07	1.00e+06	33 × 33 × 33	20	4.547	0.358	0.356	0.002	1147.100	22.412	53.281	18.337	13.187	3.539
1.10e+07	1.00e+06	65 × 65 × 65	30	6.821	0.396	0.389	0.007	990.490	26.252	58.485	21.479	14.475	0.900
1.10e+07	1.00e+06	81 × 81 × 81	30	6.821	0.395	0.388	0.007	985.690	26.406	59.487	21.605	14.723	0.299

Table 1. (continued)

Ra_{R0}	Ra_{eff}	Resolution	Q_{R0}	Q_{eff}	T_{um}	T_i	$T_{um} - T_i$	RMS Velocity	q_{surf}	q_{bot}	Nu_{surf}	Nu_{bot}	Misfit (%)
1.10e+07	1.00e+06	33×33×33	50	11.368	0.490	0.468	0.022	872.970	27.394	43.770	22.413	10.833	0.997
1.10e+07	1.00e+06	65×65×65	50	11.368	0.484	0.466	0.019	843.880	29.902	51.778	24.465	12.815	1.211
1.10e+07	1.00e+06	81×81×81	50	11.368	0.481	0.463	0.018	846.800	30.040	52.671	24.578	13.036	0.742
1.10e+07	1.00e+06	33×33×33	60	13.641	0.529	0.502	0.027	835.750	29.157	41.232	23.856	10.205	0.043
1.10e+07	1.00e+06	65×65×65	60	13.641	0.524	0.500	0.024	806.570	31.764	48.695	25.989	12.052	1.191
1.10e+07	1.00e+06	81×81×81	60	13.641	0.519	0.496	0.024	806.430	31.884	49.418	26.087	12.231	0.860
1.10e+07	1.00e+06	33×33×33	61	13.868	0.533	0.505	0.028	837.550	29.325	41.051	23.993	10.160	−0.154
1.10e+07	1.00e+06	65×65×65	80	18.188	0.600	0.566	0.034	757.240	35.712	43.253	29.219	10.705	1.161
1.10e+07	1.00e+06	65×65×65	100	22.735	0.671	0.627	0.044	724.690	39.880	38.475	32.629	9.523	1.181
1.10e+07	1.00e+06	81×81×81	100	22.735	0.668	0.625	0.043	726.200	39.859	39.276	32.612	9.721	0.494
1.10e+07	1.00e+06	65×65×65	120	27.282	0.732	0.680	0.052	713.330	44.126	34.537	36.103	8.548	0.780
1.10e+07	1.00e+06	65×65×65	140	31.829	0.790	0.731	0.060	706.860	48.613	30.842	39.774	7.633	0.806
1.10e+07	1.00e+06	81×81×81	140	31.829	0.788	0.728	0.060	699.860	48.648	31.452	39.803	7.784	0.489
1.10e+07	1.00e+06	81×81×81	160	36.376	0.841	0.775	0.067	696.920	53.137	28.008	43.476	6.932	0.396
1.10e+07	1.00e+06	65×65×65	180	40.923	0.896	0.821	0.075	692.110	57.529	23.786	47.069	5.887	0.563
1.10e+07	1.00e+06	81×81×81	180	40.923	0.893	0.818	0.075	685.970	57.639	24.360	47.159	6.029	0.448
1.10e+07	1.00e+06	65×65×65	200	45.470	0.947	0.865	0.081	692.650	62.064	20.571	50.780	5.091	0.439
3.29e+07	3.00e+06	33×33×33	0	0.000	0.235	0.226	0.008	2342.300	21.972	71.042	17.977	17.583	2.348
3.29e+07	3.00e+06	65×65×65	0	0.000	0.218	0.214	0.004	2728.300	26.027	87.600	21.295	21.681	−1.884
3.29e+07	3.00e+06	65×65×65	50	11.368	0.426	0.413	0.013	1529.100	37.125	74.501	30.375	18.439	1.954
3.29e+07	3.00e+06	65×65×65	100	22.735	0.564	0.534	0.031	1316.000	46.925	61.042	38.393	15.108	1.481
3.29e+07	3.00e+06	81×81×81	100	22.735	0.564	0.534	0.030	1313.000	47.582	63.362	38.931	15.682	1.364
3.29e+07	3.00e+06	65×65×65	120	27.282	0.614	0.577	0.036	1280.800	51.089	56.622	41.800	14.014	1.242
3.29e+07	3.00e+06	65×65×65	160	36.376	0.699	0.653	0.046	1256.100	59.534	49.002	48.710	12.128	0.432
3.29e+07	3.00e+06	65×65×65	200	45.470	0.776	0.721	0.055	1238.900	68.068	42.081	55.692	10.415	−0.353
6.58e+07	6.00e+06	33×33×33	0	0.000	0.238	0.224	0.015	2785.700	23.624	75.871	19.329	18.778	3.052
6.58e+07	6.00e+06	65×65×65	0	0.000	0.222	0.219	0.003	3813.500	31.499	106.242	25.772	26.295	−2.089
6.58e+07	6.00e+06	65×65×65	50	11.368	0.396	0.385	0.011	2256.400	42.318	90.764	34.624	22.464	2.385
6.58e+07	6.00e+06	65×65×65	120	27.282	0.549	0.520	0.029	1889.000	55.836	73.103	45.684	18.093	0.693
6.58e+07	6.00e+06	65×65×65	160	36.376	0.624	0.587	0.037	1841.100	63.897	65.321	52.279	16.167	−0.514
6.58e+07	6.00e+06	65×65×65	200	45.470	0.688	0.645	0.043	1823.400	71.819	58.481	58.761	14.474	−2.028
1.10e+08	1.00e+07	33×33×33	0	0.000	0.250	0.235	0.015	3713.000	25.166	80.638	20.590	19.958	3.279
1.10e+08	1.00e+07	129×129×129	0	0.000	0.234	0.231	0.003	5831.600	41.367	134.493	33.846	33.287	1.716
1.10e+08	1.00e+07	129×129×129	50	11.368	0.376	0.369	0.007	3036.400	50.551	119.790	41.360	29.648	0.857
1.10e+08	1.00e+07	129×129×129	120	27.282	0.515	0.494	0.022	2469.700	64.354	99.960	52.653	24.740	1.229
1.10e+08	1.00e+07	129×129×129	160	36.376	0.574	0.545	0.029	2365.100	70.614	93.030	57.775	23.025	−2.824
1.10e+08	1.00e+07	65×65×65	200	45.470	0.629	0.593	0.037	2415.100	74.174	71.386	60.688	17.668	−4.023

In aggregate, these results underline that the physics governing the internal temperatures in both planar and spherical should be (and are) identical. For direct comparison we will scale the planar system, for which the theory of *Moore* [2008] was originally developed, to its spherical equivalent. Equation (9a) and its complimentary planar form suggest that it is straightforward to compare the temperatures of basally heated systems through a constant offset. However, while accurate for basally heated systems, an additional step is needed for mixed and internally heated systems. The offset in T_{bh} corrects the reference basal heating case, but the planar system overemphasizes the effects of Q (e.g., equation (7)) and consequently temperatures. Therefore, a correction to Q is also required. For the system considered here, this correction follows $Q_{eff/spherical} = Q_{planar} \frac{(1-f^3)}{3} \frac{(1-f)}{f}$. Using this scaled Q and T_{bh} with the reported form of the T_i scale for the planar system results in $T_{scale} = 1.24 \frac{Q_{eff/spherical}^{0.75}}{Ra^{0.25}} + 0.228$. T_i results from *Moore* [2008] and *O'Farrell and Lowman* [2010] were selected for comparison. Only values of $T_i < 1.0$ were compared to avoid mantle over-heating scenarios and to minimize error (higher T_i plot at significantly increasing errors). As a result the comparison parameter ranges follow: $Ra = $ 1e5–1e7 with $Q = $ 0–30 (with $Q = $ 30 reserved for $Ra = $ 1e7, $Q = $ 10 is the maximum internal heating for $Ra < $ 1e7) [*Moore*, 2008] and $Ra = $ 1e5–1e6 with $Q = $ 5–15 [*O'Farrell and Lowman*, 2010]. The results of applying the spherical correction to the planer systems result in T_i values that are significantly lower than those predicted from the planar case but are in agreement with those predicted from spherical geometries at the scaled internal heating values (Figure 1, inset b). As a result, the temperatures are well described by the scaling relationships (misfits are nearly identical to those reported).
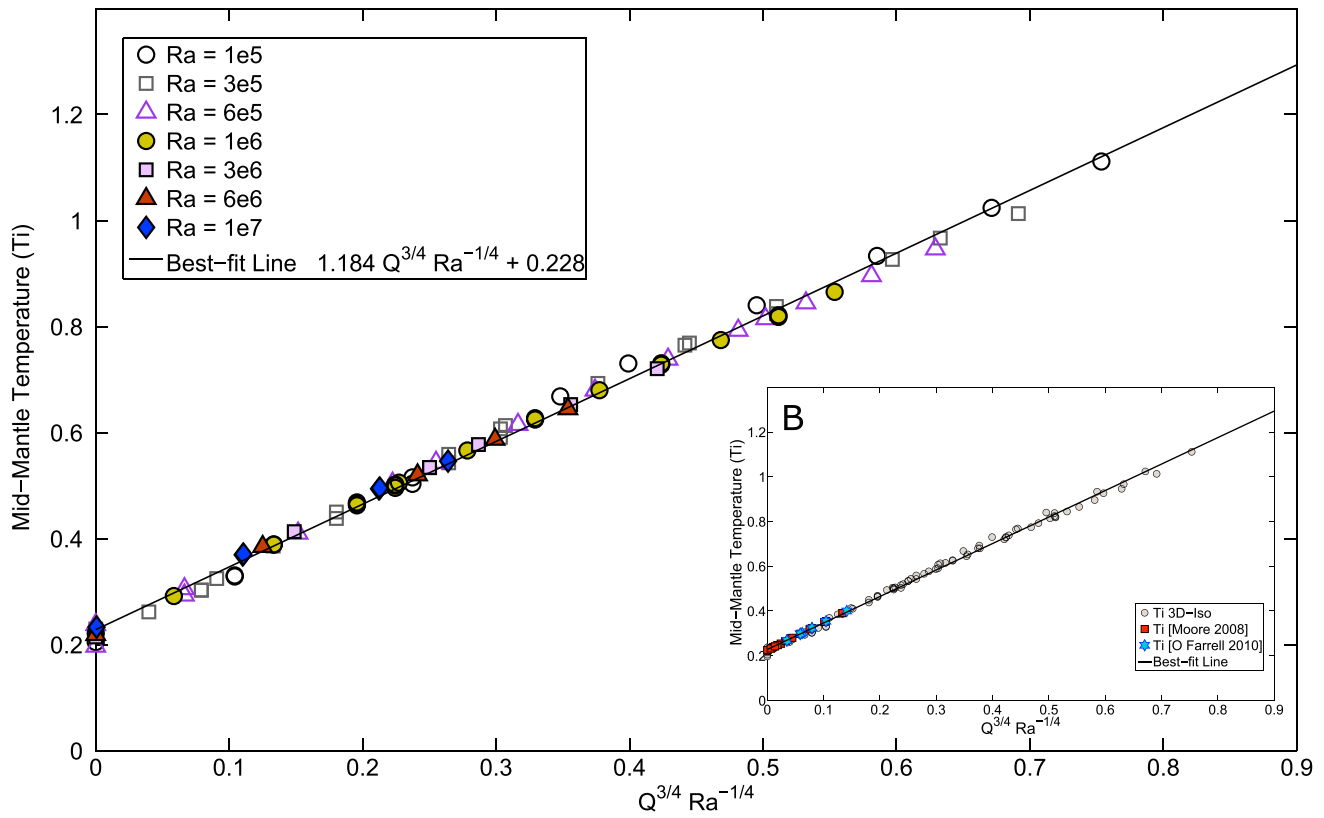
Figure 1. Internal temperature T_i versus $Q^{3/4}Ra^{-1/4}$ for the parameter ranges of Ra [1e5–1e7] and Q [0–200]. The best fit line is given by (9a). (inset b) Comparison of low-error planar results of *O'Farrell and Lowman* [2010] (blue stars) and *Moore* [2008] (red triangles), scaled to spherical geometries, to the 3-D isoviscous experiments of this study (grey circles).

An interesting aspect of mixed heating systems occurs with an inspection of temperatures for a given Q over a range of Ra. As the system Ra is increased, the relative effect of a given Q on the internal temperature decreases. Given that temperatures are well prescribed by the functional form $Q^{3/4}Ra^{-1/4}$, the change in temperature for a given Q will follow: $\Delta T \sim \Delta Ra^{-1/4}$, and indeed, this is the form that describes the differences in temperature across Ras for these experiments. Equations (9a) and (9b) can further be used to predict the Q required to give a specific temperature for a given Ra. For instance, to match the temperature of 1.12 given by a $Ra = 1e5$ and $Q_{input} = 120$, a system with a $Ra = 1e7$ would require a $Q_{input} \sim 586$. Fundamentally, even though the input Q is identical, the system will not be the same and perhaps may not even be directly comparable. It is far more useful to compare systems that exhibit the same temperatures, rather than systems that have the same level of input internal heating (this will be explored in greater detail in later sections).

5. Nusselt and Boundary Layer Scaling

The Nusselt number (Nu) is a measure of the efficiency of heat transport. We start with the scaling form outlined for the bottom heated end-member case [*Moore*, 2008]:

$$(Nu - 1) \propto (Ra - Ra_c)^{\beta}, \tag{10}$$

where $Nu \sim 1$ at the critical Ra (Ra_c) and $Nu \sim Ra^{1/3}$ for large Ra. The value for Ra_c of order 1200 is obtained from linear stability analysis [e.g., *Schubert et al.*, 2001]. Results are relatively insensitive to the choice of Ra_c, a change in the Ra_c by a factor of 2 results in less than 0.4% change in fitting parameters.

The form of the Nu scaling for a mixed heated system should approach $Ra^{1/3}$ in the limit of $Q = 0$ and large Ra, and the heat flux through the system should approach a linear dependency on Q for large Q. *Moore* [2008] assumed this later limit to scale as $Nu \sim 0.5\,Q$, with half the heat escaping through either boundary layer. This assumption requires a geometric factor for spherical systems due to the smaller area of the basal
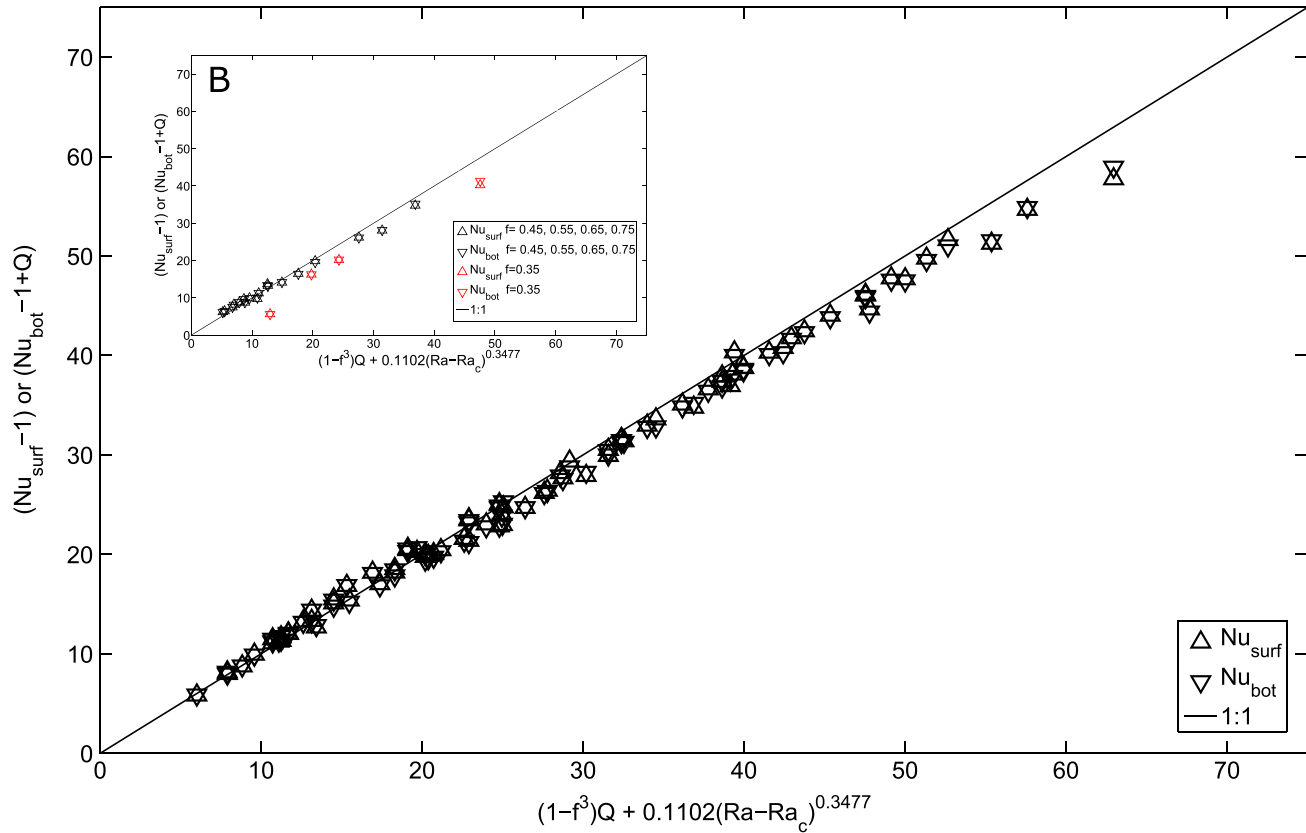
Figure 2. Simulation-determined Nusselt numbers versus predicted values at the surface (triangles) and basal boundaries (plus Q_{eff}, inverted triangles) of the system. The solid line shows a 1:1 fit that indicates a best fit empirical scaling form of $(1 - f^3)Q_{eff} + 0.1102(Ra - Ra_c)^{0.3477}$. (inset b) The fit for variable f.

boundary. It can be shown for a spherical system of geometry f that the geometric Q prefactor should scale by a form of $1 - f^3$. Combining equations (8) and (10) and the prefactor term, the heat flow can be seen to follow:

$$(Nu_{surf} - 1) = (Nu_{bot} - 1) + Q_{eff} = (1 - f^3)Q_{eff} + \alpha(Ra - Ra_c)^\beta \tag{11}$$

A critical aspect of *Moore*'s [2008] theory is that it did not assume that a $\beta = 1/3$ scaling will hold over the full range of Q and Ra that is applicable to the thermal histories of terrestrial planets. This breaks from the traditional view established through *Howard* [1966]. The traditional view is that the dynamics of the upper boundary layer can be treated as being self-determined such that the upper boundary layer does not "see the shear stresses exerted by the interior flow (to leading order), and therefore, the thermal boundary layer structure is completely self-determined" [*Fowler*, 1985]. *Moore* [2008] argued that for Q and Ra conditions of the present-day Earth, boundary layer dynamics would not be in a self-determined regime but would instead fall into a boundary layer interaction regime with, for example, rising hot thermals interacting with the upper thermal boundary layer and effecting its dynamic stability (this would lead to a deviation from a $\beta = 1/3$ scaling). That argument is supported by earlier numerical experiments, in planar geometry, which indicated that a *Howard* [1966] scaling could be retrieved only for Ra exceeding a value of 10^9 [*Lenardic and Moresi*, 2003]. The associated Nu value, from the experiments of *Lenardic and Moresi* [2003], beyond which a $\beta = 1/3$ scaling could be retrieved was between 50 and 60. Determining the degree to which the spherical shell case shows similar departures from self-determined boundary layer dynamics is a motivation of this paper.

We can obtain a best regression fit of all our numerical results onto equation (11), not accounting for the prediction that the results might span transitions between different regimes of boundary layer dynamics. If we do so, the best fit that follows is given by

$$(Nu_{surf} - 1) = (Nu_{bot} - 1) + Q_{eff} = (1 - f^3)Q_{eff} + 0.1102(Ra - Ra_c)^{0.3477} \tag{12}$$

Table 2. Variable f

Ra_{R0}	Ra_{eff}	Resolution	f	Q_{R0}	Q_{eff}	q_{surf}	q_{bot}	Nu_{surf}	Nu_{bot}	Misfit (%)
3.29e+06	3.00e+05	33 × 33 × 33	0.55	0	0.000	11.956	39.535	9.782	9.785	−0.028
3.29e+06	3.00e+05	33 × 33 × 33	0.55	4	0.909	13.389	40.295	10.955	9.973	0.731
3.29e+06	3.00e+05	33 × 33 × 33	0.55	12	2.728	14.997	38.644	12.270	9.564	−0.201
3.29e+06	3.00e+05	33 × 33 × 33	0.55	20	4.547	17.470	38.898	14.294	9.627	0.905
3.29e+06	3.00e+05	33 × 33 × 33	0.55	61	13.868	25.541	27.056	20.897	6.696	1.684
3.29e+06	3.00e+05	33 × 33 × 33	0.55	99	22.508	33.275	18.680	27.225	4.623	0.359
3.29e+06	3.00e+05	33 × 33 × 33	0.55	148	33.648	43.747	10.312	35.793	2.552	−1.164
3.29e+06	9.04e+05	33 × 33 × 33	0.35	0	0.000	3.597	29.083	6.681	6.616	1.138
3.29e+06	9.04e+05	33 × 33 × 33	0.35	12	7.110	9.318	44.611	17.305	10.149	0.282
3.29e+06	9.04e+05	33 × 33 × 33	0.35	20	11.850	11.421	41.152	21.211	9.362	−0.006
3.29e+06	9.04e+05	33 × 33 × 33	0.35	61	36.143	22.223	27.162	41.271	6.179	−2.577
3.29e+06	5.48e+05	33 × 33 × 33	0.45	0	0.000	8.801	44.517	10.757	11.018	−2.640
3.29e+06	5.48e+05	33 × 33 × 33	0.45	12	4.443	12.408	43.402	15.165	10.742	−0.144
3.29e+06	5.48e+05	33 × 33 × 33	0.45	20	7.406	14.332	40.364	17.517	9.990	0.736
3.29e+06	5.48e+05	33 × 33 × 33	0.45	61	22.587	23.820	26.542	29.113	6.569	−0.154
3.29e+06	1.41e+05	33 × 33 × 33	0.65	0	0.000	15.796	37.537	8.506	8.540	−0.449
3.29e+06	1.41e+05	33 × 33 × 33	0.65	12	1.562	18.313	36.275	9.861	8.253	0.519
3.29e+06	1.41e+05	33 × 33 × 33	0.65	20	2.604	19.907	35.276	10.719	8.025	0.928
3.29e+06	1.41e+05	33 × 33 × 33	0.65	61	7.942	27.341	28.344	14.722	6.448	2.447
3.29e+06	5.14e+04	33 × 33 × 33	0.75	12	0.771	21.689	33.977	7.230	6.371	1.424
3.29e+06	5.14e+04	33 × 33 × 33	0.75	20	1.285	22.414	32.540	7.471	6.101	1.325
3.29e+06	5.14e+04	33 × 33 × 33	0.75	61	3.918	27.697	27.703	9.232	5.194	1.461

The Q prefactor terms median value is reported as 0.8069 (±0.1177), which is nearly identical to the expected $1 - f^3$ scaling form for $f = 0.55$. Additional f values were tested ($f = 0.35 - 0.75$; Figure 2, inset b, and Table 2), with nearly identical fits ($f = 0.35$ begins to deviate slightly from this trend), indicating $1 - f^3$ is a robust scaling form. The best fit scaling relationship indicates the exponent β ranges from 0.3181 to 0.3773 (within 95% confidence interval; Table 3), with 0.3477 as the median case. The numerical trends indicate that this best fit empirical scaling value is predominantly sampling different Nu-Ra regimes, a higher Ra "weak boundary

Table 3. Scaling Relationships

| Value		Scaling	R^2
		Upper Mantle and Surface	
T_{um}		$0.223 + 1.335\, Q_{sc}^{3/4}\, Ra^{-1/4}$	0.9979
	coefficients (95%)	0.223 (±0.0047)	
	coefficients (95%)	1.335 (±0.0140)	
$(Nu_{surf} - 1)$ or $(Nu_{bot} - 1 + Q)$		$0.8069\, Q_{sc} + 0.1102\, (Ra - Ra_c)^{0.3477}$	0.9953
	coefficients (95%)	0.8069 (±0.1177)	
	coefficients (95%)	0.1102 (±0.0477)	
	exponents (95%)	0.3477 (±0.0296)	
δ_{surf}		$T_{um}/(Nu_{surf})$	0.9795
		Interior	
T_i		$0.228 + 1.184\, Q_{sc}^{3/4}\, Ra^{-1/4}$	0.9965
	coefficients (95%)	0.228 (±0.0054)	
	coefficients (95%)	1.184 (±0.0160)	
ΔT		$0.1774\, Q_{sc}\, Ra^{-1/3}$	0.9773
	coefficients (95%)	0.1774 (±0.0125)	
Velocity		No one scale	NA
		Mantle Base	
$Nu_{bot} - 1$		$-0.1931\, Q_{sc} + 0.1102\, (Ra - Ra_c)^{0.3477}$	0.9775
	coefficients (95%)	−0.1931 (±0.1177)	
	coefficients (95%)	0.1102 (±0.0477)	
	exponents (95%)	0.3477 (±0.0296)	
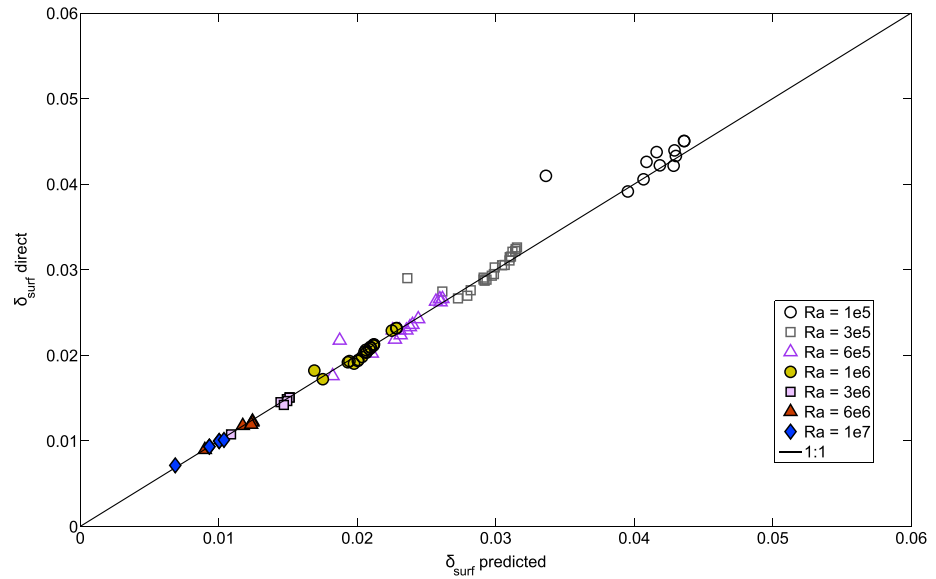
Figure 3. Surface boundary layer thicknesses versus predicted boundary layer thicknesses. The solid line indicates a 1:1 fit.

layer (BL) interaction" regime in which β is approaching 1/3, an intermediate Ra "transitional BL interaction regime," and a lower Ra "strong BL interaction" regime which is predicted to deviate more strongly from the classic $\beta = 1/3$ value [e.g., *Moore*, 2008]. High Nu values in Figure 2 ($Nu - 1 > 50$) show a deviation from the $\beta = 0.3477$ trend and instead are fit well by a β that approaches 1/3, in agreement with the 2-D numerical results of *Lenardic and Moresi* [2003] for the same Nu range. For $20 < Nu - 1 \leq 50$ the system is in a transitional BL interaction regime with a $\beta \cong 0.34$. In the range of $Nu - 1 \leq 20$, the system operates within a strong BL interaction regime, where $\beta \cong 0.35$. Subset β values for weak, transitional, and strong BL interaction regimes have larger best fit ranges due to smaller sample sizes and cannot be determined nonuniquely; however, the best fit values indicated fall within the 95% confidence interval of the overall best fit empirical trend indicating that the single fit bulk trend is indeed sampling multiple physics related to multiple interaction regimes. Similar to the high Nu cases for $f = 0.55$ the deviation for $f = 0.35$ in Figure 2 (inset b) is nearly completely accounted for by allowing β to approach 1/3.

We now seek a scaling form of the boundary layer thickness (δ) as a function of both Ra and Q. As shown in (9b), our T_{um} is comparable to ΔT_{top} defined in *Moore* [2008] to describe the temperature drop across the upper boundary layer. The predicted form of δ_{surf} for spherical systems becomes

$$\delta_{surf} = \frac{T_{um}}{Nu_{surf}} = \frac{0.223 + 1.335 Q^{3/4} Ra^{-1/4}}{\left(1 - f^3\right) Q + 0.1102 \left(Ra - Ra_c\right)^{0.3477}} \tag{13}$$

The predicted form of the scaling is shown versus the δ_{surf} from simulations in Figure 3. The degree of fit is given by $R^2 = 0.987$ for all Ra ranges. The average variance between predicted to actual is 2.6%. The data points that deviate from the prediction occur when $Q = 0$ (pure basal heating) and at low Ra. Removing these data points, results in an improvement of fit with an $R^2 = 0.996$. Generally, the fit improves as both Ra and Q increase as systems with both low Ra and low Q exhibit long period oscillations in system parameters (Figures 4a and 4b), consistent with oscillatory regimes indicated from laboratory experiments [e.g., *Davaille and Limare*, 2007 and references therein].

A specific prediction follows from equations (12), (13), (9a), and (9b), that the surface heat flow and boundary layer thickness do not exhibit a 1:1 functional relationship. Comparing the output heat flow and surface boundary layer thickness from our numerical experiments in Figure 5 confirms this. It is useful to compare boundary layer data with a boundary layer Rayleigh number (Ra_b) defined as $Ra_b = Ra \Delta T_b$, where ΔT_b is the temperature drop across the boundary layer, given by T_{um} in our models. Ra_b is a more robust indicator of internal dynamics linked to surface characteristics than quantities such as $Ra_Q(RaQ)$. The boundary layer thickness has a power law dependency on Ra_b, and for clarity two fits are indicated, basal and high Q
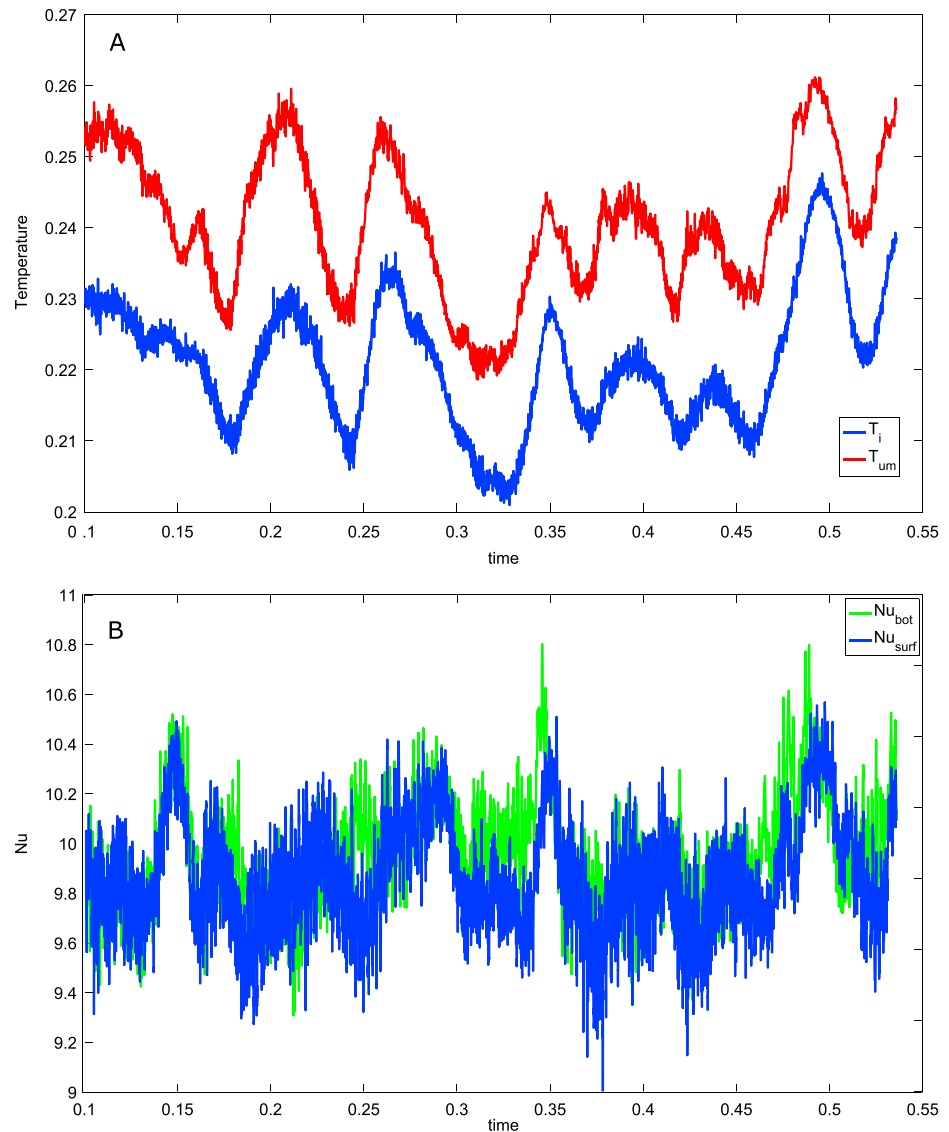
Figure 4. Variable long wavelength output for $Ra = 1e5$ ($Q = 0$). Time series of (a) internal temperatures and (b) Nu values.

asymptotic. For basally heated systems, the best fit exponent is -0.388 (Figure 6a, solid line), different than the classic $-1/3$ value. The fit is robust with $R^2 = 0.959$. With the addition of internal heating, a change in boundary layer behavior is observed. At high levels of internal heating ($Q > 50$ for $Ra < 1e6$ and $Q > 100$ for $Ra > 1e6$), boundary layers begin to converge to an asymptotic limit. This high Q asymptotic limit indicates a best fit exponent of -0.359 (Figure 6a, dashed line), with an $R^2 = 0.985$. Overall, the effects of increasing the system Ra (at a constant Q value) lead to a decrease in ΔT_b and δ_{surf} that are well prescribed by scaling relationships. However, the effects of increasing the internal heating rate (at a constant Ra) are less straightforward, as the system exhibits two distinct behaviors. It can be anticipated that some deviation from pure basal and high internal heating cases should be expected, with the intermediate internal heating case ($0 < Q \leq \sim 50$ for $Ra < 1e6$ and $0 < Q \leq 100$ for $Ra > 1e6$) indicating some form of system adjustment as the system resides in neither end-member state. As internal heating increases from a basally heated condition for low Q, the boundary layer thickness increases with increasing Ra_b. However, as the system approaches an internally heated state, it begins to approach an asymptotic value and enters a regime where subsequent increasing internal heating (and Ra_b) decreases boundary layer thicknesses along the asymptotic line. The same behavior can be seen in the 2-D planar data of *Moore* [2008]. This behavior is consistent with the isoviscous convective planform metastability suggested by *Arrial et al.* [2014].
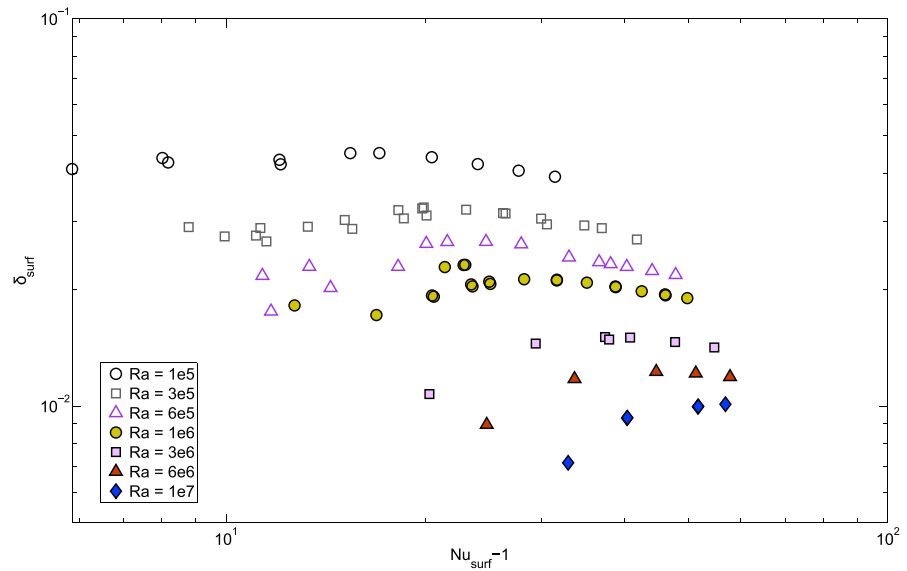
Figure 5. $Nu_{surf} - 1$ versus surface boundary layer thicknesses (δ) for experiment space.

Given the complexity in the δ_{surf} relationship, it is worth inspecting how heat flow changes with Ra_b. For pure basally heated systems in the limit of high Ra, we expect that $Nu \sim Ra^{1/3}$ [e.g., *Turcotte and Schubert*, 2005] or alternately that $Nu_{surf} - 1 \sim \left(\frac{Ra\Delta T_b}{Ra_c\Delta T}\right)^{1/3}$. Results of $Nu_{surf} - 1$ versus Ra_b are illustrated in Figure 6b. In the limit of no internal heating, the best fit line describing $Nu_{surf} - 1$ follows a power law slope of 0.362 with Ra_b (solid line Figure 6b), which deviates from the theoretical scaling of 1/3, but is well described with an $R^2 = 0.990$ and is consistent with the relationships shown previously. The best fit exponent does not remain constant with increasing internal temperatures. At high internal heating ($Q_{input} = 160$), the exponent of the best fit changes to a value of 0.131 (omitted from Figure 6b for clarity). However, as was shown in section 4, this is misleading. The systems are not being affected by a given Q in the same way. This makes a direct comparison difficult as the parameter ranges explored may not allow for completely comparable temperatures. Therefore, to compare systems appropriately, the internal temperature should be matched, not the level of internal heating. However, the effects of Q (noting the previous limitation) can be explored within a given Ra. In bulk, the system appears to be approaching a Ra specific asymptote. As the system experiences increased heating, the surface heat flow shows a decreasing dependency on Ra_b. The break in behavior is given by an onset Q, which scales as $Ra_b^{0.284}$ (dashed line Figure 6b) and corresponds to the asymptotic Q limit identified in Figure 6a. Inspecting the behaviors of low (pre-onset) Q and high (post-onset) Q in Figures 6a and 6b indicates that the dependency of quantities such as heat flow and boundary layer dynamics on internal parameters is complex. At low internal heating, both the boundary layer and the heat flow increase roughly linearly. Above the onset Q value, surface heat flow increases while the boundary layer thickness decreases. However, the predicted scaling form of onset Q intersects the basal heating trend at $Nu_{surf} - 1 \sim 116$ and $Ra_b \sim 9e7$, indicating and that traditionally identified (classic) scaling forms (such as $Nu \sim \delta^{-1}$ [e.g., *Solomatov*, 1995]) are applicable for all levels of internal heating for a system of $Ra > \sim 4e8$. However, for an $Ra < 4e8$, the system fundamentally allows for differing scaling behaviors linked to different regimes (strong/weak BL interaction, classic). This in turn allows for multiple expressions of $Nu_{surf} - 1$ for the same value of δ_{surf} (or vice versa), suggesting that the surface heat flow may not always be a reliable metric to determine lithosphere thicknesses of planets.

We turn our attention to the behavior of the basal boundary. A specific prediction from the scaling theory is that changes in the heat flow of the upper boundary should be reflected in some inverse form by the lower boundary layer. This behavior is illustrated in Figure 6c. In the limit of no internal heating, the best fit scaling form describing $Nu_{bot} - 1$ follows a power law slope of 0.362 with Ra_b (Figure 6c, solid line), which is identical to the scaling form of $Nu_{surf} - 1$. Similar to Figure 6b, as the system experiences increasing levels of heating, the basal heat flow shows a decreasing dependency on Ra_b. Generally, while surface heat flow increases,
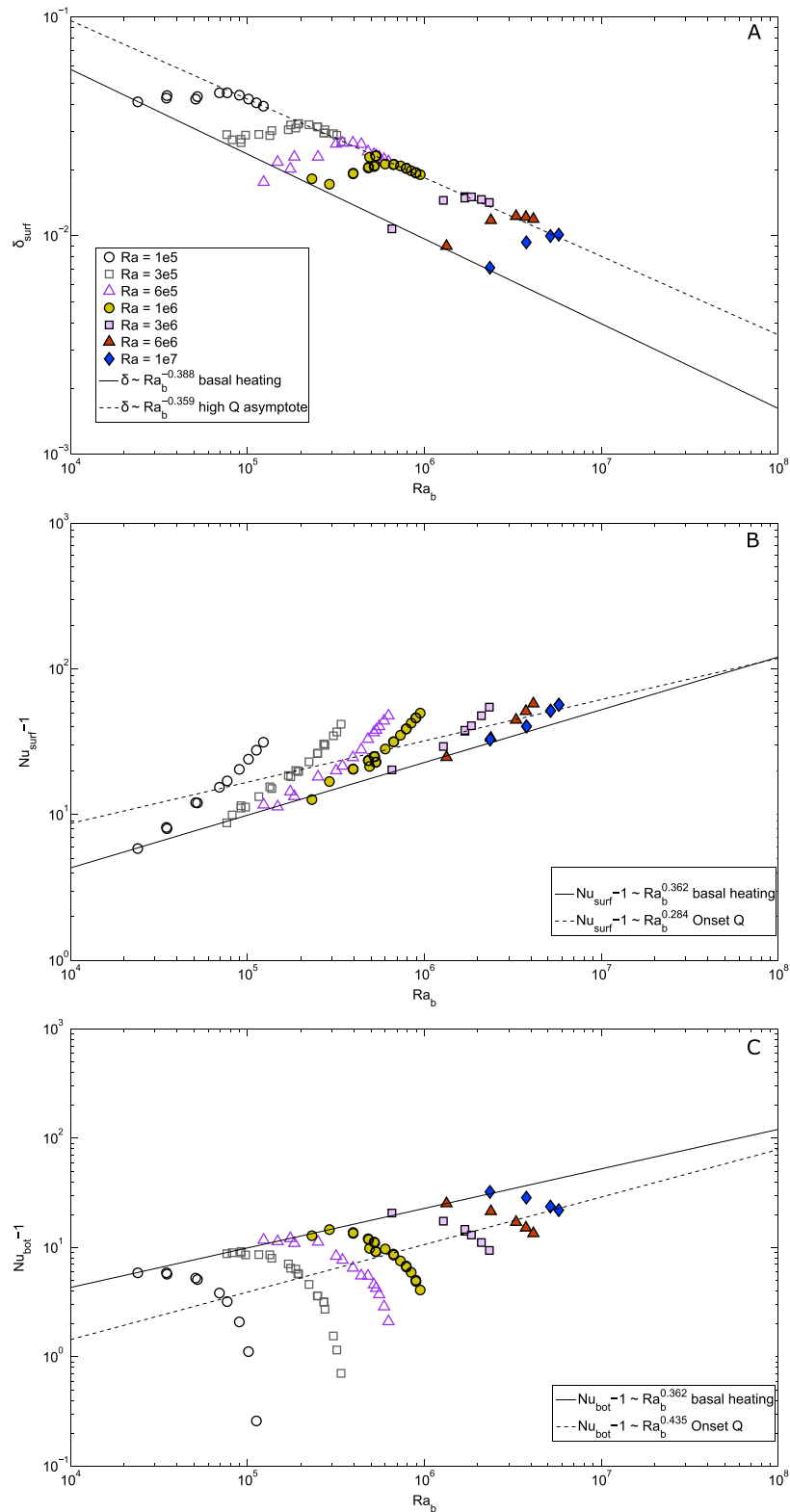
Figure 6. (a) Surface boundary layer thickness (δ) versus boundary layer Rayleigh number ($Ra_b = Ra\Delta T_b$); (b) surface heat flux ($Nu_{surf} - 1$) versus boundary layer Rayleigh number; and (c) basal heat flux ($Nu_{bot} - 1$) versus boundary layer Rayleigh number. A range of internal heating rates is plotted for each Ra result. The solid line is a fit to bottom heated cases, whereas dashed lines indicate the onset Q, where δ values in Figure 6a become asymptotic, indicating the transition between a high-Ra "low-boundary layer (BL) interaction" regime and a low-Ra "strong BL interaction" regime.

basal heat flow decreases. The differences in system behavior, given by the onset Q, are more pronounced, and the trend, given as $Nu_{bot} - 1 \sim Ra_b{}^{0.435}$ (dashed line Figure 6c), indicates an equal but opposite change in the exponent form from Nu_{surf}, validating the prediction of inverse activity between the boundaries.

An additional prediction from scaling theory, in planar cases, is that an increase in internal heating should force the boundary layers to become asymmetric (e.g., increasing the heat flow of the upper boundary, while decreasing the heat flow across the lower boundary). However, in spherical cases the boundaries are already asymmetric (~83% of the heat flow is through the surface boundary; equation (12)). As a result, higher temperature behaviors (e.g., basal heat fluxes become negative) should occur for lower values of temperature (and conversely higher values of Q) than *Moore* [2008] reported due to the effect of a spherical geometry. This implies the scaling form of critical Q (the Q for which $Nu_{bot} \rightarrow 0$), which is reported in the form $Q = (0.15 - 0.35)Ra^{1/3}$ for planar cases [*Moore*, 2008], would be predicted to scale with a different exponent due to geometric effects. Indeed, the form is predicted from data to scale as $Q_{sc} = (1.836 \pm 0.572)Ra^{(0.257 \pm 0.0207)}$, indicating that spherical geometries require larger internal heating rates than planar counterparts would predict.

6. Temperature Gradient Scaling

The temperature profile in internal and mixed heating systems is not, in general, expected to be constant with depth. In internally heated convection, distributed upwelling flow is a passive response to concentrated downwelling of cold upper boundary layer material. Passive upwellings balance the mass flux of active downflows from the upper boundary layer. As fluid from depth moves upward to replace material from the active surface boundary layer, internal heating in the system gradually increases the parcel's temperature. This asymmetry between upflows and downflows, which do not heat significantly on descent, can lead to a subadiabatic gradient within the interior of the convecting layer [*Jeanloz and Morris*, 1987]. The temperature gradient with depth is expected to be proportional to the heating rate and inversely proportional to upwelling velocities [e.g., *Turcotte and Schubert*, 2005].

To explore subadiabatic scalings from our experiments, we tracked the difference in temperature between upper and lower mantles ($\Delta T = T_{um} - T_i$). This is directly analogous to the dT/dz employed in *Moore* [2008]. The best fit curve in the 2-D planar numerical experiments of *Moore* [2008] was associated with subadiabatic gradient that scaled as $(QRa^{-1})^{0.52}$. From a theory point of view, this was close to the expectation if upwelling velocity scaled as the internally heated Rayleigh number to the 1/2 power which leads to a predicted subadiabatic gradient scaling given by $(QRa^{-1})^{0.50}$. The theoretical upwelling velocity scale used by *Moore* [2008] comes from the assumption that the upwelling velocity will scale as the downwelling velocity and that the downwelling velocity scale will follow the form associated with a sinking fluid sheet that remains steadily attached to the upper boundary layer [e.g., *O'Neill et al.*, 2007].

Figure 7 shows that the scaling form of *Moore* [2008] provides a poor fit to our 3-D spherical results (bulk $R^2 = 0.5056$). While at high Q there is scaling form that can be recovered, it is both Ra specific and indicates a power law slope of 1.347 ± 0.192 ($R^2 > 0.990$ within a given Ra). Though it is clear that there exists a sensitivity to the Q/Ra scale, it strongly deviates from the form that stems from assuming an upwelling velocity scale that balances a steady conduit type downwelling (see Figure 7, inset b, for comparison with the 2-D planar case of *Moore* [2008]). The alternative possibility to steady conduit flow is a velocity scaling associated with discrete drips [e.g., *O'Neill et al.*, 2007]. In that case the vertical velocity will scale as $Ra^{1/3}$. Figure 7c indicates that the results collapse to single trend for moderate and high values of Q, with a best fit line of $0.1774 \, Q/Ra^{1/3}$ within a high level of agreement ($R^2 = 0.9556$). It should be noted that a similar, though lower, quality fit can be achieved by allowing the vertical velocity to scale with $Ra^{1/4}$ ($R^2 \sim 0.92$). However, the $Ra^{1/3}$ scale is preferred given both the more robust fit of $Ra^{1/3}$ to the data and that there is currently no obvious physical reason to explain why the vertical velocity would scale as $Ra^{1/4}$.

Of interest is another departure from the planar scaling cases. For high Q, the gradient is indeed subadiabatic. However, for low values of Q ($Q_{input} < 10$) the gradient may be weakly negative, indicating the existence of a superadiabatic profile. At low Ra ($<1e6$), there appear to be two distinct temperature gradient trends operating opposite in slope to each other. From $Q = 0$ to $Q_{input} \sim 10$, the profiles indicate a decrease in temperature gradient with increasing Q. At $Q_{input} \sim 10$, a minimum in the temperature gradient occurs, after which
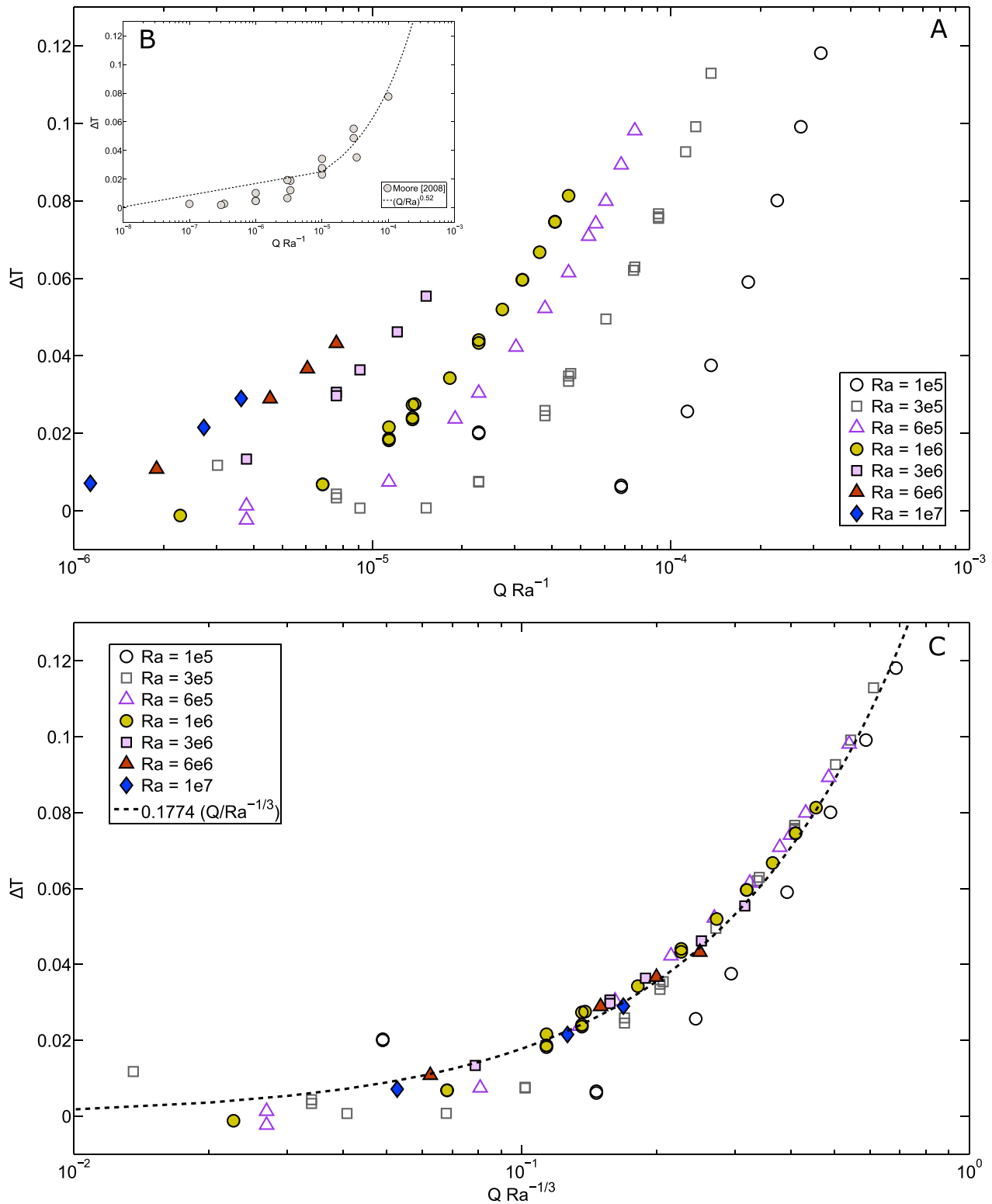
Figure 7. The temperature gradient of the mantle plotted against a functional form of Q and Ra. $\Delta T = T_{um} - T_i$ is directly analogous to dT/dz from *Moore* [2008]. (a) 3-D isoviscous results plotted against the form of Q/Ra, predicted from internal heating velocity scaling, with poor agreement ($R^2 = 0.5056$). (b) Inset shows results of *Moore* [2008] (grey circles), with a best fit form of $16 (Q/Ra)^{0.52}$, in agreement with internal heating scaling predictions (e.g., steady conduit flow of $Ra_Q^{1/2}$). (c) 3-D isoviscous results plotted against the discrete drip velocity scale (e.g., $Ra^{1/3}$), with a best fit form of $0.1774 \, Q/Ra^{1/3}$ and high level of agreement ($R^2 = 0.9556$) for $Q > 10$. The form is subadiabatic for high Q and high Ra but deviates strongly at low Q for low Ra systems ($Ra < 1e6$). From $Q = 0$ to $Q \sim 10$, systematic decreases in ΔT to slightly superadiabatic values are possible and are a consequence of curvature and 3-D geometries. All plots are semilog.
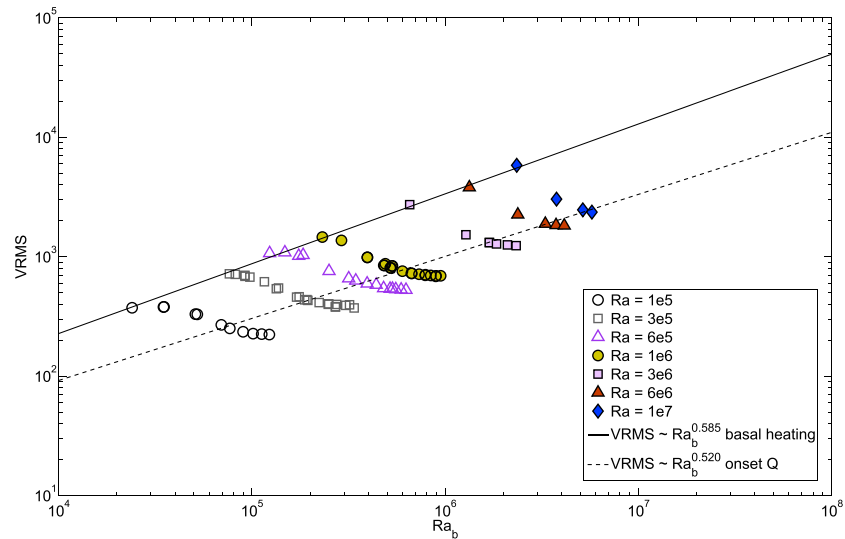
Figure 8. Internal velocities (VRMS) versus boundary layer Rayleigh number ($Ra_b = Ra\Delta T_b$). A range of internal heating rates are plotted for each Ra result. The solid line is a fit to bottom heated cases, whereas dashed lines indicate the onset Q, where δ values in Figure 6a become asymptotic, indicating the transition between a high-Ra "low Boundary Layer (BL) interaction" regime and a low-Ra "strong BL interaction" regime.

gradients increase. In general, these results suggest that a single fit in temperature gradients in a spherical parameter space that operates across multiple regions of boundary layer interactions (e.g., strong, weak, and classic) should not be expected—similar to our conclusion regarding Nusselt number scalings.

7. Velocity Scaling

The original theory of *Moore* [2008] showed a ΔT that was well described by a scaling form that assumed a steady conduit flow velocity. Aside from that, the work did not consider velocity scaling further. Our results indicate that the vertical velocity scaling differs between 2-D planar and 3-D spherical with the former scaling associated with conduit flow and the later with discrete thermals. This is perhaps not a surprise given that 2-D planar geometry forces the system toward cellular rolls that have sheet-like downflows. That geometry also limits time-dependent cell structure which can minimize the potential for development of discrete sinking drips. We turn now from vertical velocity to the bulk system RMS velocity. As indicated in Figure 8, the RMS velocity has a power law dependency on Ra_b, similar to both Nu and δ scaling obtained previously. For basally heated systems, the best fit exponent is 0.585 which falls below the classic theoretical scaling of exponent 2/3 [e.g., *Schubert et al.*, 2001]. However, this fit is a bulk trend over high and low Ra. Subselecting the parameter range toward high Ra ($Ra \geq 1e6$) results in fits approaching two-thirds scaling, with a best fit exponent of 0.63.

While velocities are predicted to increase with increasing Ra for a fixed level of internal heating, the system exhibits more complex behavior for varying levels of internal heating at any given Ra. Values of velocity approach asymptotes at both high and low levels of internal heating. Intermediate levels of internal heating indicate rapid system adjustments between the asymptotes, with the dividing value given as the onset Q (as defined in Figure 6a) with a predicted scaling form of $Ra_b^{0.520}$. This predicts that in high Q systems (or high T_i regimes) RMS velocities plateau and that further increasing heating or temperature will not result in increasing RMS velocities, despite increasing surface heat flux and decreasing boundary layer thickness (Figure 6b).

As outlined, ΔT has an interdependence on velocity. The results of the velocity and ΔT scale from Figure 7c are explored (Figure 9). Best fit trends for a given Q along variable Ra are indicated. The data are well described ($R^2 > 0.999$) by a power law relationship where the slopes approach -1.55 for high Q. The utility of this form is that for a given internal heating rate and given ΔT, the velocity may be predicted (or vice versa) following $V_{RMS} \sim \Delta T^{1.55}$ for high Q or $\Delta T^{1.58}$ for intermediate Q (provided $Q > 10$). Similar to Figure 8, for a fixed Ra over variable Q despite a first-order reduction in velocity, there appear to be different subtrends
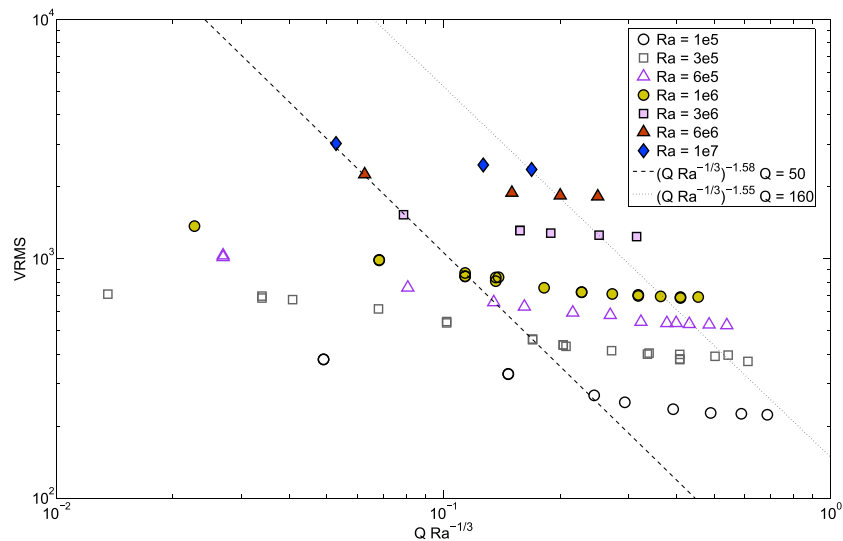
Figure 9. Internal velocities (VRMS) versus $QRa^{-1/3}$ scale. Dashed line indicates moderate levels of internal heating ($Q = 50$) and the dotted line indicates high levels of internal heating ($Q = 160$).

in the data, and no single scaling form can completely fit, or describe, the data. It is interesting to note as Q increases for a given Ra, the temperature gradients increase, but the velocities themselves become asymptotic. This may indicate that the convecting mantle is becoming sluggish in response to the stable density layering associated with a strongly subadiabtic thermal gradient (i.e., cold high-density mantle below warmer lower density upper mantle). This is a prediction that can be tested by examining the scaling relationship of velocity with heat flow and boundary layer dynamics.

The system velocity can be shown to scale with heat flow along a certain range of Q (Figures 10a and 10b). We can recast the heat flow as a function of velocity. The surface heat flow is well described by a similar power law relationship as was expressed in Figure 8 (Figure 10a). For low levels of Q, $Nu_{surf} - 1$ varies with velocity by a power law of 0.618 (basal heating) to 0.606 (high Q). The same susceptibility to differing internal heating rate effects as a function of Ra (similar to Figure 6) occurs for the higher Q range. However, the asymptotic regimes from Figure 8 indicate a change in behavior given by onset Q which scales as $Nu_{surf} - 1 \sim VRMS^{0.534}$. Figure 10b shows a dependency of basal boundary heat flux on velocity, by a near-identical scaling form as the surface boundary for low Q systems. At high Q, this form breaks down. This indicates that the upper and lower boundary layers are connected by the RMS velocity, highlighting that the system is operating within a strong BL interaction regime for low Q parameters. As the system evolves to higher temperatures and levels of internal heating, the basal boundary heat flux also becomes independent of the RMS velocity (a direct inverse relationship with the surface), given by onset Q ($Nu_{bot} - 1 \sim VRMS^{0.838}$). This may suggest that BLs are decoupling. Therefore, the increase in heat flux must come from surface boundary layer dynamics alone.

Figure 11 shows RMS velocity versus surface boundary layer thickness. As expected, velocity scales inversely to δ_{surf}, with a best fit power law slope of -1.460 for basal heating and -1.811 (omitted from Figure 11 for clarity) for high internal heating rates. The bulk system behavior (best fit exponent for all simulations) is nearly parallel with the basal heating case, with a slope of -1.512. As was suggested by Figures 10a and 10b, the increasing surface heat flow and increasing internal temperatures with near-constant RMS velocities are being accommodated by a rapidly thinning boundary layer. This suggests that in high-temperature regimes the convective system can only remove heat by boundary layer thinning associated in response to a hotter mantle. Prior to that point, the system can adjust characteristic flow wavelengths and associated RMS velocity, in order balance heat flow with heat production. After that RMS velocities plateau, the boundary layer itself balances heat flow with heat production until it is physically thin enough to be indistinguishable from the interior of the mantle. If this later state exists in planetary convective systems, it would likely be very short-lived and perhaps not existent at all given that the high temperatures associated with it would favor a heat pipe mode of convection which would change the system scalings [*Moore and Webb*, 2013].
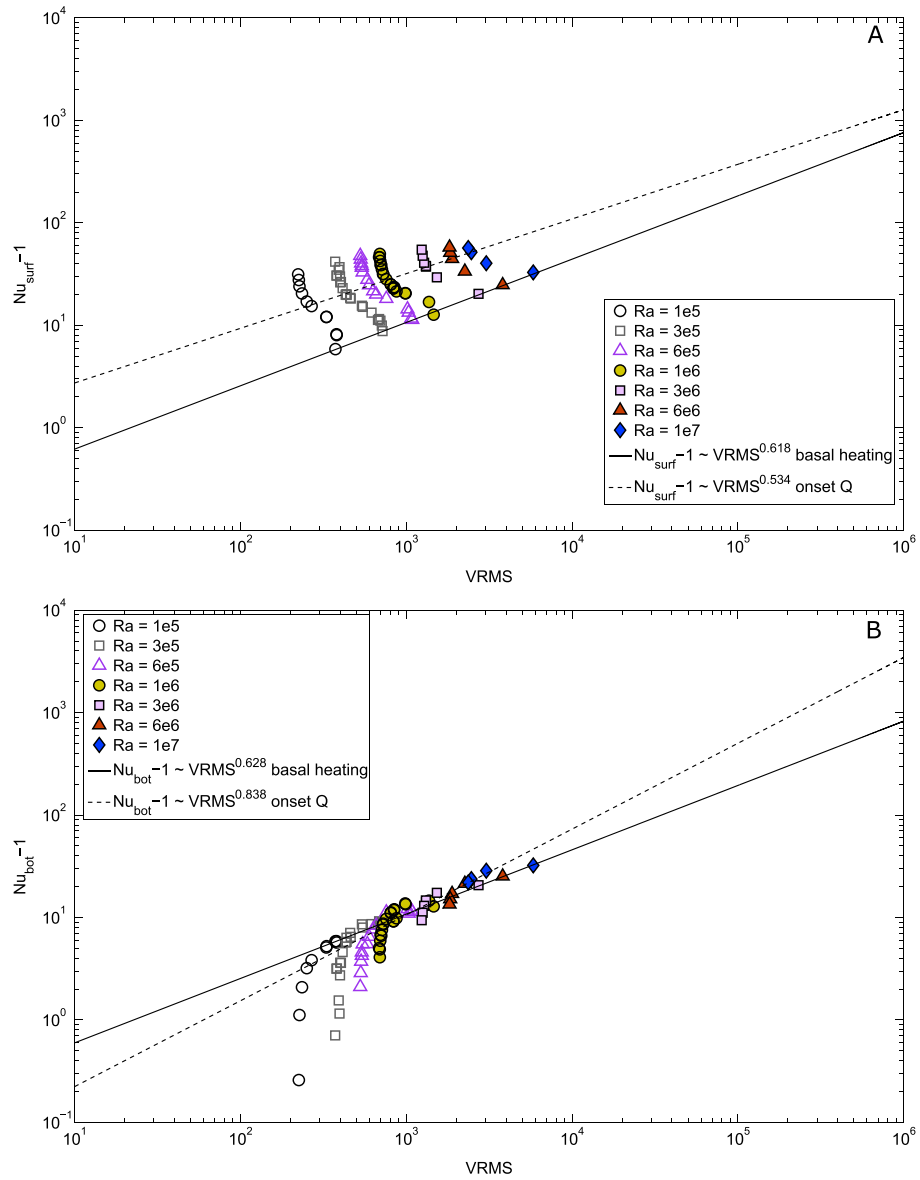
Figure 10. (a) Surface heat flux ($Nu_{surf} - 1$) versus internal velocities (VRMS) and (b) basal heat flux ($Nu_{bot} - 1$) versus internal velocities (VRMS). A range of internal heating rates are plotted for each Ra result. The solid line is a fit to bottom heated cases, whereas dashed lines indicate the onset Q, where δ values in Figure 6a become asymptotic, indicating the transition between a high-Ra "low boundary layer (BL) interaction" regime and a low-Ra "strong BL interaction" regime.

8. Discussion

The dynamics and heat transfer properties of mixed heating thermal convection have previously been explored for one-, two-, and three-dimensional systems with different viscosity formulations [e.g., *Sotin and Labrosse*, 1999; *Reese et al.*, 1999; *Hauck and Phillips*, 2002; *Reese et al.*, 2005; *Moore*, 2008; *Shahnas et al.*, 2008; *Choblet and Parmentier*, 2009; *O'Farrell and Lowman*, 2010; *Deschamps et al.*, 2010; *Choblet*, 2012; *O'Farrell et al.*, 2013]. This study has tested and extended the isoviscous 2-D planar theoretical heat transfer scalings of *Moore* [2008] to 3-D spherical systems (Table 3). Internal temperatures (T_i) and boundary layer temperature drops (T_{um}) are well described by the modified scalings adjusted for spherical geometries. Surface heat flux retains a linear form of simple addition of internally generated heat to that of heat transported by the temperature difference between the boundaries reported by *Moore* [2008], modified to account for curvature at the base of the mantle. Scaling theory-predicted boundary layer thicknesses agree
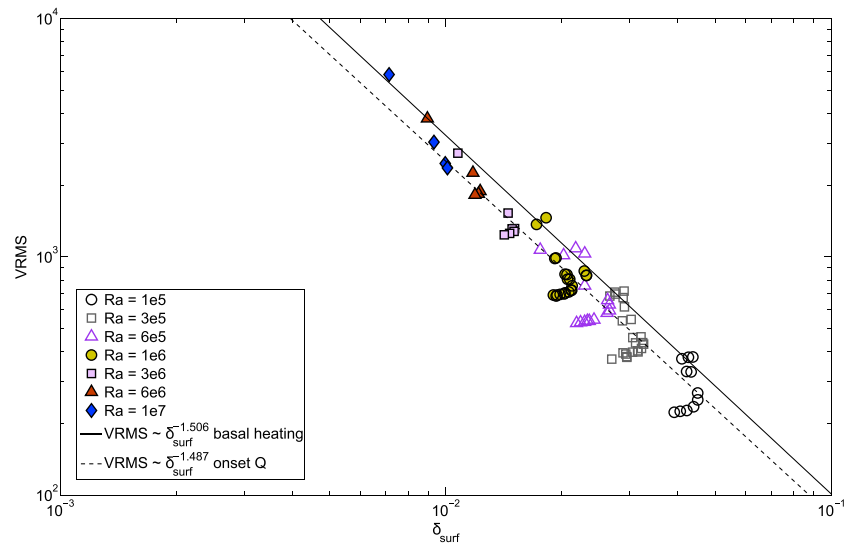
Figure 11. Internal velocities (VRMS) versus surface boundary layer thickness (δ). A range of internal heating rates are plotted for each Ra result. The solid line is a fit to bottom heated results, whereas dashed lines indicate the onset Q, where δ values in Figure 6a become asymptotic, indicating the transition between a high-Ra "low boundary layer (BL) interaction" regime and a low-Ra "strong BL interaction" regime.

with numerical experiment-derived thicknesses to a high degree of accuracy. Internal mantle temperature gradients are well predicted by a modified form of the *Moore* [2008] scaling that accounts for differences in vertical velocity between 2-D planar and 3-D spherical cases.

Our results show that conversion between temperatures in planar and spherical geometries can be accomplished via appropriate geometric conversions. Care should be taken when comparing planar and spherical geometry results at the same parameter values. Instead of directly comparing systems with similar input parameters, our results highlight that it is of greater utility to compare systems operating at the same, or close to equivalent, internal temperatures.

The results of our study reinforce and reemphasize a critical departure of mixed heated convection dynamics from local boundary layer stability theory [e.g., *Christensen*, 1989; *Lenardic and Moresi*, 2003; *Moore*, 2008]. Specifically, *Howard*'s [1966] (classic) theory does not apply to convective systems until Nu exceeds ~50. At this limit, the scaling exponent for heat flux versus Ra converges toward one third. For the parameter ranges considered in this study, the bulk exponent best fit is 0.3477. It should be reemphasized that this Nu scaling exponent is a single empirical fit over regions of differing system dynamics, and as a result, it is misleading to apply a single fit across all Nu values.

Any discussion of mantle temperature gradients is intertwined with that of internal velocities. Our results show a mismatch between 2-D planar scalings for the internal mantle temperature gradient, which assume vertical velocity scalings appropriate for conduit flow. Instead, the gradients from our 3-D spherical experiments are well described (for high Ra and Q) by a vertical velocity scaling appropriate for discrete drip flow. This discrepancy appears to be tied both to curvature and to the extra degree of freedom provided by 3-D geometries. Two general trends exist for RMS velocities: (1) Velocities increase with increasing basal Ra and (2) velocities decrease with increasing Q. The first case is consistent qualitatively with the bottom heated convective scale of $V_{\mathrm{rms}} \propto Ra^{2/3}$, thus ensuring that for a given internal heating rate, an increase in Ra will increase internal velocities. However, the second trend is less expected. If we consider planets, it is easy to show that the Ra should change much more slowly than the internal heating (more closely following trend 2) over a planet's radiogenic lifetime. This implies that high Q (early) planets have lower bulk internal velocities than later, cooler, planets. This in turn would predict that stresses, linked to internal velocities, could be lowest early in a planet's development despite the overall higher Ra state. This would indicate that for any system in which radiogenic are important, simple bottom heated and pure internal heating scaling laws and extrapolations [e.g., *Valencia et al.*, 2007; *Valencia and O'Connell*, 2009] can be misleading (see *Weller and*

Lenardic [2016] for a more thorough discussion). This offers another line of support, in addition to viscosity arguments, for models that predict lower stress states (stagnant lids) early in planetary development [e.g., *O'Neill and Lenardic*, 2007; *Weller and Lenardic*, 2012; *Lenardic and Crowley*, 2012; *Stein et al.*, 2013; *Weller et al.*, 2015].

Of interest is understanding why low Q (low T_i) systems have higher convective velocities than high Q systems. *O'Farrell and Lowman* [2010] noted this behavior and suggested that it reflected a transition to more diffuse upwellings. We expand on this idea and suggest that these quantities can also be influenced by the characteristic wavelength of mantle flow (which is free to evolve in spherical models).

A line of evidence that the wavelength of mantle flow structure can have a strong effect on heat flow and temperature distribution comes from the results of *Höink and Lenardic* [2010] and *Arrial et al.* [2014]. *Höink and Lenardic* [2010] showed that internal temperatures can vary as much as 30% with a variance in aspect ratio in planar geometries, a value that is nearly identical to that obtained from *Arrial et al.* [2014] of ~25% from spherical geometries. It should be noted that similar results can be seen from the steady state solutions of differing aspect ratios reported by *O'Farrell and Lowman* [2010].

Considering the dependence of aspect ratio on internal quantities, a decrease in velocity with increasing Q is qualitatively expected, as are maximal velocities for basally heated systems. For isoviscous convection, increased internal heating moves the system toward smaller cell aspect ratios [*Schubert and Anderson*, 1985] which are associated with lower average velocities. As internal heating increases, the temperature drop from the upper to the lower mantle increases due to the development of a subadiabatic thermal profile. The net effect is a stable density layering which can decrease convective vigor and has the potential to alter characteristic flow wavelengths. How temperature- and/or depth-dependent viscosity alters these results in a 3-D sphere remains an open question for future work. Currently, no scaling theory exists that can predict coupled aspect ratio, velocity, and temperature gradient development as a function of heat production in 3-D spheres.

Many numerical modeling suites are currently not set up to explicitly track aspect ratios over time in spherical 3-D. Our results suggest that this is a worthwhile future avenue. Analog experiments could also be of value to test both 3-D spherical aspect ratio development, as well as the shell-derived heat flow conversion equation (section 3). Using current spherical core experiments [e.g., *Aurnou and Olson*, 2001], direct measurements of heat flow for defined geometries and modifications to the experiments could be made in order to directly test and validate a subset of our numerical results.

Our 3-D spherical scalings will be expanded in the future to include temperature-dependent viscosity, depth-dependent viscosity, and lid states with yielding. Convection within a high-viscosity contrast regime differs from isoviscous convection in that the temperature-dependent viscosity modifies the temperature drop across the convecting region to a rheological temperature scale that is of order 1 [e.g., *Davaille and Jaupart*, 1993], which forces this layer into the small viscosity contrast regime, whereas the bulk internal mantle is that of nearly isoviscous convection. *Ra* adjustments in this sublayer then can only respond by changing the mean temperature and consequently the viscosity. Depth-dependent viscosity formulations, in contrast, allow for more subtle changes from pure isoviscous convection, such as a weak *Ra* dependence on mean temperature in basally heated convective systems [*O'Farrell et al.*, 2013] and longer wavelength dependence on aspect ratio [*Bunge et al.*, 1996]. Yielding formulations, using both temperature- and depth-dependent viscosity allow for mobility of the surface and interaction with the interior despite high viscosity "lids." These updated scalings, built upon the fundamental framework of isoviscous convection, can be applied to complex convective systems that more closely emulate planetary development.

References

Arrial, P. A., N. Flyer, G. B. Wright, and L. H. Kellogg (2014), On the sensitivity of 3-D thermal convection codes to numerical discretization: A model intercomparison, *Geosci. Model Dev.*, *7*(5), 2065–2076.
Aurnou, J. M., and P. L. Olson (2001), Rotating magnetoconvection experiments in liquid gallium, *J. Fluid Mech.*, *430*, 283–307.
Bunge, H. P., M. A. Richards, and J. R. Baumgardner (1996), The effect of depth-dependent viscosity on the planform of mantle convection, *Nature*, *379*, 436–438.
Choblet, G. (2012), On the scaling of heat transfer for mixed heating convection in a spherical shell, *Phys. Earth Planet. Inter.*, *206–207*, 31–42.
Choblet, G., and E. M. Parmentier (2009), Thermal convection heated both volumetrically and from below: Implications for predictions of planetary evolution, *Phys. Earth Planet. Inter.*, *173*, 290–296.
Christensen, U. R. (1989), The heat transport by convection rolls with free boundaries at high Rayleigh number, *Geophys. Astrophys. Fluid Dyn.*, *46*, 93–103.

Davaille, A., and C. Jaupart (1993), Transient high-Rayleigh-number thermal convection with large viscosity variations, *J. Fluid Mech.*, *253*, 141–166.

Davaille, A., and A. Limare (2007), Laboratory studies of mantle convection, *Treatise Geophys.*, *7*, 89–165.

Deschamps, F., P. J. Tackley, and T. Nakagawa (2010), Temperature and heat flux scalings for isoviscous thermal convection in spherical geometry, *Geophys. J. Int.*, *182*, 137–154.

Deschamps, F., C. Yao, P. J. Tackley, and C. Sanchez-Valle (2012), High Rayleigh number thermal convection in volumetrically heated spherical shells, *J. Geophys. Res.*, *117*, E09006, doi:10.1029/2012JE004090.

Fowler, A. C. (1985), A mathematical model of magma transport in the asthenosphere, *Geophys. Astrophys. Fluid Dyn.*, *33*, 63–96, doi:10.1080/03091928508245423.

Hauck, S. A., and R. J. Phillips (2002), Thermal and crustal evolution of Mars, *J. Geophys. Res.*, *107*(E7), 5052, doi:10.1029/2001JE001801.

Höink, T., and A. Lenardic (2010), Long wavelength convection, Poiseuille-Couette flow in the low-viscosity asthenosphere and the strength of plate margins, *Geophys. J. Int.*, *180*, 23–33, doi:10.1111/j.1365-246X.2009.04404.x.

Howard, L. N. (1966), Convection at high Rayleigh number, in *Proceedings of the 11th International Congress on Applied Mechanics*, edited by H. Gortler, pp. 1109–1115, Springer, New York.

Jeanloz, R., and S. Morris (1987), Is the mantle geotherm subadiabatic, *Geophys. Res. Lett.*, *14*, 335–338, doi:10.1029/GL014i004p00335.

Lenardic, A., and J. W. Crowley (2012), On the notion of well-defined tectonic regimes for terrestrial planets in this solar system and others, *Astrophys. J.*, *755*(2), 132.

Lenardic, A., and L. Moresi (2003), Thermal convection below a conducting lid of variable extent: Heat flow scalings and two-dimensional, infinite Prandtl number numerical simulations, *Phys. Fluids*, *15*(2), 455–466.

Moore, W. B. (2008), Heat transport in a convecting layer heated from within and below, *J. Geophys. Res.*, *113*, B11407, doi:10.1029/2006JB004778

Moore, W. B., and A. A. G. Webb (2013), Heat-pipe Earth, *Nature*, *501*, 501–505.

O'Neill, C., and A. Lenardic (2007), Geological consequences of super-sized Earths, *Geophys. Res. Lett.*, *34*, L19204, doi:10.1029/2007GL030598.

O'Farrell, K. A., and J. P. Lowman (2010), Emulating the thermal structure of spherical shell convection in plane-layer geometry mantle convection models, *Phys. Earth Planet. Int.*, *182*, 73–84, doi:10.1016/j.pepi.2010.06.010.

O'Farrell, K. A., J. P. Lowman, and H.-P. Bunge (2013), Comparison of spherical shell and plane-layer mantle convection thermal structure in viscously stratified models with mixed-mode heating: Implications for the incorporation of temperature-dependent parameters, *Geophys. J. Int.*, *192*, 456–472, doi:10.1093/gji/ggs053.

O'Neill, C., A. M. Jellinek, and A. Lenardic (2007), Conditions for the onset of plate tectonics on terrestrial planets and moons, *Earth Planet. Sci. Lett.*, *261*, 20–3.

Reese, C. C., V. S. Solomatov, and L. N. Moresi (1999), Non-Newtonian stagnant lid convection and magmatic resurfacing on Venus, *Icarus*, *139*, 67–80.

Reese, C. C., V. S. Solomatov, and J. R. Baumgardner (2005), Scaling laws for time-dependent stagnant lid convection in a spherical shell, *Phys. Earth Planet. Inter.*, *149*(3–4), 361–370.

Schubert, G., and C. A. Anderson (1985), Finite element calculations of very high Rayleigh number thermal convection, *Geophys. J. R. Astron. Soc.*, *80*, 575–602.

Schubert, G., D. L. Turcotte, and P. Olson (2001), *Mantle Convection in the Earth and Planets*, Cambridge Univ. Press, New York.

Shahnas, M. H., J. P. Lowman, G. T. Jarvis, and H.-P. Bunge (2008), Convection in a spherical shell heated by an isothermal core and internal sources: Implications for the thermal state of planetary mantles, *Phys. Earth planet. Int.*, *168*, 6–15.

Solomatov, V. S. (1995), Scaling of temperature- and stress-dependent viscosity convection, *Phys. Fluids*, *7*, 266–274.

Sotin, C., and S. Labrosse (1999), Three-dimensional thermal convection in an iso-viscous, infinite Prandtl number fluid heated from within and from below: Applications to the transfer of heat through planetary mantles, *Phys. Earth Planet. Inter.*, *112*(3–4), 171–190.

Stein, C., J. P. Lowman, and U. Hansen (2013), The influence of mantle internal heating on lithospheric mobility: Implications for super-Earths, *Earth Planet. Sci. Lett.*, *361*, 448–459, doi:10.1016/j.epsl.2012.11.011.

Tan, E., E. Choi, P. Thoutireddy, M. Gurnis, and M. Aivazis (2006), Geoframework: Coupling multiple models of mantle convection within a computational framework, *Geochem. Geophys. Geosyst.*, *7*, Q06001, doi:10.1029/2005GC001155.

Turcotte, D. L., and G. Schubert (2005), *Geodynamics*, 2nd ed., Cambridge Univ. Press, New York.

Valencia, D., and R. J. O'Connell (2009), Convection scaling and subduction on Earth and super-Earths, *Earth Planet. Sci. Lett.*, *286*, 492–502, doi:10.1016/j.epsl.2009.07.015.

Valencia, D., R. J. O'Connell, and D. Sasselov (2007), Inevitability of plate tectonics on super-Earths, *Astrophys. J.*, *670*, L45, doi:10.1086/524012.

Weller, M. B., and A. Lenardic (2012), Hysteresis in mantle convection: Plate tectonics systems, *Geophys. Res. Lett.*, *39*, L10202, doi:10.1029/2012GL051232.

Weller, M. B., A. Lenardic, and C. O'Neill (2015), The effects of internal heating and large scale climate variations on tectonic bi-stability in terrestrial planets, *EPSL*, 85–94, doi:10.1016/j.epsl.2015.03.021.

Weller, M. B., and A. Lenardic (2016), The energetics and convective vigor of mixed-mode heating: Velocity scalings and implications for the tectonics of exoplanets, *Geophys. Res. Lett.*, *43*, doi:10.1002/2016GL069927.

Wolstencroft, M., J. H. Davies, and D. R. Davies (2009), Nusselt–Rayleigh number scalingfor a spherical shell Earth mantle simulation up to a Rayleigh number of 109, *Phys. Earth Planet. Int.*, *176*, 132–141.

Zhong, S., M. T. Zuber, L. Moresi, and M. Gurnis (2000), Role of temperature-dependent viscosity and surface plates in spherical shell models of mantle convection, *J. Geophys. Res.*, *105*, 11,063–11,082, doi:10.1029/2000JB900003.

Zhong, S., A. K. McNamara, E. Tan, L. Moresi, and M. Gurnis (2008), A benchmark study on mantle convection in a 3-D spherical shell using CitcomS, *Geochem. Geophys. Geosyst.*, *9*, Q10017, doi:10.1029/2008GC002048.